

Dorado and its member galaxies. III

Mapping star formation with FUV imaging from UVIT. ★

R. Rampazzo^{1,2}, P. Mazzei², A. Marino², L. Bianchi³, J. Postma⁴,
R. Ragusa⁵, M. Spavone⁵, E. Iodice⁵, S. Ciroi⁶, and E.V. Held²

¹ INAF-Osservatorio Astrofisico di Asiago, Via dell'Osservatorio 8, 36012 Asiago, Italy e-mail: roberto.rampazzo@inaf.it

² INAF-Osservatorio Astronomico di Padova, Vicolo dell'Osservatorio 5, 35122 Padova, Italy

³ Dept. of Physics & Astronomy, The Johns Hopkins University, 3400 N. Charles St., Baltimore, MD 21218, USA

⁴ University of Calgary, 2500 University Drive NW, Calgary, Alberta, Canada

⁵ INAF-Osservatorio Astronomico di Capodimonte, Salita Moiariello 16, 80131 Napoli, Italy

⁶ Department of Physics and Astronomy "G. Galilei", University of Padova, Vicolo dell'Osservatorio 3, 35122 Padova, Italy

April 6, 2022 ; May 30, 2022

ABSTRACT

Context. We are investigating the star formation in galaxies of the actively evolving Dorado group where, for a large fraction of both early- and late-type galaxies, signatures of interactions and merging events are revealed by optical and radio observations.

Aims. Our previous $H\alpha+[N II]$ study, probing ≈ 10 Myrs timescales, suggested that star formation is still ongoing in early-type galaxies. In this work, we use far-UV (FUV) imaging to map recent star formation on longer times scales, of the order of 100 Myrs.

Methods. We used the Ultraviolet telescope UVIT on board *Astrosat* to image the galaxies of the Dorado backbone previously observed in $H\alpha+[N II]$, with the far-UV filter FUV.CaF2 (1300-1800 Å). The sample includes NGC 1536, NGC 1546, NGC 1549, [CMI2001]4136-01, NGC 1553, IC 2058, PGC 75125, NGC 1566, NGC 1596 and NGC 1602; for the two latter galaxies, the UVIT data provide the first view in far-UV. For the others, previously observed by GALEX, the UVIT data afford a $\sim 5\times$ improvement in spatial resolution.

Results. FUV.CaF2 emission is revealed in all the Dorado galaxies observed, tracing young stellar populations in ring structures and showing tidal distortions. The Sérsic index, derived by fitting the luminosity profiles, is always $n < 3$ suggesting that the FUV.CaF2 emission originates from a disk also in early-type galaxies. The star formation rate (SFR) ranges from $0.004\pm 0.001 M_{\odot} \text{yr}^{-1}$ of [CMI2001]4136-01 to $2.455\pm 0.027 M_{\odot} \text{yr}^{-1}$ of NGC 1566. Most of the recent star formation is found at the periphery of the Dorado group where most of late-type galaxies are located. For these galaxies, the ratio $\text{SFR}_{H\alpha}/\text{SFR}_{\text{FUV.CaF2}}$ is close to 1, except for the edge-on IC 2058, similarly to previously reported relations for Local Volume samples. For early-type galaxies, however, $\text{SFR}_{H\alpha}$ is about 15 times higher than SFR_{FUV} . The Dorado's early-type galaxies define a separate locus in $\text{SFR}_{\text{FUV}}, \text{SFR}_{H\alpha}$ space with respect to the late-type galaxies, which is well represented by the relation $\log(\text{SFR}_{\text{FUV.CaF2}}) = 0.70 \times \log(\text{SFR}_{H\alpha}) - 1.26$.

Conclusions. The disk structure of the FUV.CaF2 emitting populations discovered in all the early-type galaxies implies dissipative processes and wet merging events. The systematic discrepancy between SFRs derived from $H\alpha$ and FUV fluxes suggests that rejuvenation episodes in early-type galaxies cannot sustain constant star formation over ~ 100 Myrs timescales.

Key words. Ultraviolet: galaxies – Galaxies: elliptical and lenticular, cD – Galaxies: spiral – Galaxies: interaction – Galaxies: evolution

1. Introduction

In the Local Supercluster (LS, $\leq 3500 \text{ km s}^{-1}$) (de Vaucouleurs 1953) galaxy groups play an important role in the galaxy evolution. Kourkchi & Tully (2017) suggested that, considering the infall domain of LS, only a small fraction of the galaxy mass resides within clusters. Virgo, Fornax and Antlia associations with an infall mass of $7\times 10^{14} M_{\odot}$, $2\times 10^{14} M_{\odot}$ and $4\times 10^{14} M_{\odot}$ respectively, contain 60%, 30% and 15% of their mass already collapsed within the cluster (Kourkchi & Tully 2017). This evidence suggests that a large fraction of galaxies in the LS are still evolving within small galaxy associations, making the study of groups critical to understand galaxy evolution.

Before groups fall into clusters, they collapse under gravity forming substructures where their galaxy members undergo a morphological transformations, as for early-type galaxies (ETGs), and start to quench. A number of studies shows that ETGs are more strongly clustered than late-type galaxies (LTGs)

(Davis & Geller 1976; Dressler 1980). Boselli & Gavazzi (2014) reviewed some of the mechanisms driving galaxy evolution as a function of the environment. Such mechanisms act transforming field galaxies, i.e. LTGs, into cluster-like galaxies, i.e. ETGs, and drive groups from an *active* (star forming) phase, typical of the field, (see e.g. Marino et al. 2016; Rampazzo et al. 2018) to a more *passive* phase, typical of the clusters. It is widely admitted that cluster galaxies tend to have depressed star formation (SF) in comparison to the field (see e.g. Bressan et al. 2006; Poggianti et al. 2006; Rampazzo et al. 2013, and references therein). At least part of the galaxy transformation happens at densities typical of the groups, i.e. groups operate a galaxy pre-processing.

We are investigating galaxy groups, from Local Group Analogs (Marino et al. 2010, 2013, 2014) to very evolved group, as NGC 5486 groups (Marino et al. 2016) using a multi-wavelength approach to understand their evolution exploring the connection between their galaxy population and their activity.

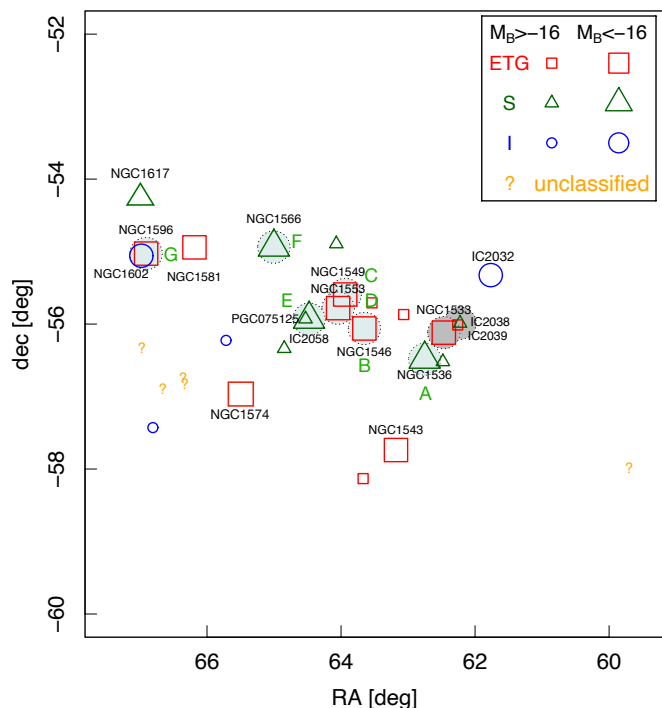


Fig. 1. Projected distribution of Dorado galaxy members according to Firth et al. (2006) and Kourkchi & Tully (2017). Members are labelled according to their morphology and B-Band magnitude provided by HyperLeda. UVIT FUV.CaF2 fields listed in Table 1, are enclosed by a light-green circle having the diameter of the UVIT field ($28'$). Target galaxies within each field are also labelled. The morphological, photometric and star forming properties obtained from the UVIT FUV.CaF2 data-set about NGC 1533, IC 2038/2039, dark-grey circles in the figure, have been presented and discussed in in Ram2021. Ram2020 also observed NGC 1581 and NGC 1543 in $H\alpha + [N II]$. All galaxies but the NGC 1596/NGC 1602 have been already observed with GALEX at lower resolution and sensitivity (see e.g. Marino et al. 2011a,b).

This paper continues our study, in optical (Cattapan et al. 2019) in $H\alpha$ (Rampazzo et al. 2020, hereafter Ram2020) and FUV (Rampazzo et al. 2021, hereafter Ram2021), of the Dorado group and its sub-structures.

Dorado is a nearby (17.69 Mpc) group in the Southern Hemisphere (RA=64.3718 deg, Dec=-55.7811 deg). We adopt the member list defined by Firth et al. (2006, and reference therein) and Kourkchi & Tully (2017) (see Table A.1 of Ram2020). Figure 1 shows the projected distribution of Dorado members, indicating their morphological class and B-band magnitude. Multi-wavelength data, from FUV to optical and radio, converge in presenting Dorado as a strongly evolving group of galaxies in the LS. A large fraction of Dorado members, including ETGs, shows either merging or interaction signatures in their structures (Section 2 in Ram2020). Residual SF is seen in bright ETGs that populate the red sequence as well as in intermediate luminosity members still crossing the green valley of the UV-optical colour magnitude diagram of the group (see Figure 1 in Cattapan et al. 2019).

Dorado has a clumpy structure (Firth et al. 2006) with respect to evolved groups, e.g. NGC 5486 (Marino et al. 2016).

Iovino (2002) found that the central part of Dorado forms a compact group, namely SGC 0414-5559, composed of the brightest galaxies at the peak of the velocity distribution (Table A.1 in Ram2020). This structure, the core of Dorado, is formed by NGC 1546, NGC 1549, NGC 1553 and IC 2058. Compact groups are the ideal sites to study galaxy interactions and mergers given the high space density and low velocity dispersions of their galaxies (Mamon 1992). From N-body simulations Diaferio et al. (1994) proposed that compact groups continuously form within loose groups during their collapse and virialization phase. There are several observational evidences that compact groups are found within looser structures or rich neighbourhoods (see e.g. Ribeiro et al. 1998, and references therein). Diaferio et al. (1994) simulations suggested that the life time of the compact groups is about 1 Gyr and most of the simulated member galaxies are not merger remnants. More recently, semi-analytic simulations (SAMs) by Díaz-Giménez et al. (2021) suggested a late assembly for the compact groups which may host merger remnants. This could be the case of SGC 0414-5559 in Dorado, since both NGC 1549 and NGC 1553 show a wide shell system (Malin & Carter 1983).

Some peripheral sub-structures have been evidenced in Dorado, as the triplet formed by NGC 1533, IC 2039 and IC 2039 (Cattapan et al. 2019), South-East of the compact group. Pair-like structures as NGC 1566/NGC 1581 (Kendall et al. 2015; Oh et al. 2015) and NGC 1596/NGC 1602 (Bureau & Chung 2006; Chung et al. 2006) are found North-West of the compact group. Most of these galaxies show signatures of interaction as discussed by Ram2020.

A further indication that Dorado is at an early stage of evolution is the fact that it is still gas-rich when compared to evolved environments. The basic ingredient for SF, $H I$ reservoirs, have been revealed in several Dorado members (Ryan-Weber et al. 2003; Kilborn et al. 2009; Elagali et al. 2019), with the exclusion of NGC 1549 and NGC 1553. There are signatures of gas transfer between the LTG NGC 1602 and the ETG NGC 1596 (Chung et al. 2006). The fuel to ignite SF in the ring of the lenticular galaxy NGC 1581 (Ram2020) may have been stripped by the interaction (Oh et al. 2015; Kendall et al. 2015) with NGC 1566.

Ram-pressure stripping signatures of $H I$ have been detected in NGC 1566 (Elagali et al. 2019). This is particularly interesting since the galaxy is located at the periphery of the Dorado group. The presence of ram-pressure stripping has long been suggested to operate in removing gas from spirals in rich clusters (Gunn & Gott 1972) but its efficiency was questioned in less rich environments (Abadi et al. 1999). Kantharia et al. (2005) revealed signatures in the radio continuum and 21 cm $H I$ observations of both tidal interaction and ram-pressure stripping on spiral members of Holmberg 124, a poor group environment. Roberts et al. (2021) extended the search for jelly-fish galaxies in low density environments in the radio continuum domain with the LOFAR Two-metre Sky Survey (LoTSS) project investigating about 500 SDSS groups ($z < 0.05$). They find that jelly-fish galaxies are most commonly found in clusters, with the frequency decreasing towards the lowest-mass groups. Vulcani et al. (2021) provided a panorama about different processes taking place in low-density environments, including ram-pressure stripping, with VLT/MUSE optical data. The *GALaxy evolution EXplorer* (GALEX hereafter) (Martin et al. 2005; Morrissey et al. 2007) was used to identify asymmetries, as tails and jelly-fish tentacles, by Smith et al. (2010) in Coma galaxies, as well as to study star formation in jelly-fish tentacles in single objects in Virgo (see e.g. Hester et al. 2010, references

Table 1. Dorado galaxies observed with UVIT

Field centre	ID	RA (J2000)	Dec (J2000)	GALEX FUV [AB mag]	V_{hel} km s ⁻¹	Morpho. Type	M_B	R_{25} arcsec	PA deg	ϵ
A	NGC 1536	04 11 00.53	-56 29 05.6	16.03±0.01 ¹	1296	5.0	-17.80	49.8	162.6	0.28
B	NGC 1546	04 14 36.46	-56 03 39.2	17.36±0.02 ¹	1238	-0.4	-19.24	111.5	144.8	0.32
C	NGC 1549	04 15 45.13	-55 35 32.1	17.06±0.05 ³	1202	-4.3	-20.61	153.9	146.2	0.15
	[CMI2001]4136-01	04 16 15.43	-55 41 49.2
D	NGC 1553	04 16 10.50	-55 46 49.0	16.73±0.05 ³	1201	-2.3	-21.02	189.3	150.4	0.31
				16.32±0.13 ²	1201	-2.3	-21.02			
E	IC 2058	04 17 54.30	-55 55 58.0	16.15±0.03 ²	1397	6.5	-17.55	95.0	17.9	0.85
			0	16.24±0.02 ⁴						
	PGC 075125	04 18 07.10	-55 55 50.0	...	1369	5.0	-15.81	16.9	27.8	0.26
F	NGC 1566	04 20 00.42	-54 56 16.1	12.13±0.02 ⁴	1504	4.0	-20.89	217.3	44.2	0.32
G	NGC 1596	04 27 38.1	-55 01 40.1	...	1510	-2.0	-19.27	116.7	19.3	0.73
G	NGC 1602	04 27 54.9	-55 03 28.1	...	1740	9.5	-17.87	55.9	88.5	0.48

Notes. Col.1 gives the UVIT fields; Col. 2 the galaxy identification. Members of Dorado, according to Kourkchi & Tully (2017) are indicated in bold face; Col.s 3 and 4 give Right Ascension and Declination; Col. 5 the FUV apparent asymptotic magnitude, not extinction corrected, from: (1) GALEX archive, Bai et al. (2015), (3) Simonian & Martini (2017) and (4) Gil de Paz et al. (2007). Col. 6, Col.7 and Col. 8 lists the heliocentric radial velocity, the galaxy morphological type and the absolute B-band magnitude, respectively by Kourkchi & Tully (2017) which adopted for all the galaxies the distance of 17.69 Mpc. Col. 9, Col. 10 and Col. 11 provide the radius at $\mu_B=25$ mag arcsec⁻², and the corresponding Position Angle and ellipticity from HyperLeda. The source indicated with [CMI2001]4136-01 has been already revealed by GALEX and detected in H α + [N II] by Rampazzo (2020), showing that it is a member of Dorado.

therein). More recently, high spatial resolution FUV studies using Astrosat-UVIT investigated ram-pressure stripping in action in cluster jelly-fish galaxies (George et al. 2018; Hota et al. 2021).

This paper presents our study of the Dorado backbone based on Astrosat-UVIT FUV.CaF2 observations. We investigate the central compact group SGC 0414-5559 and the two sub-structures formed by NGC 1566/NGC 1581 and NGC 1596/NGC 1602. Target galaxies are listed in Table 1. We associated to the FUV.CaF2 images two deep optical, g and r -bands wide field images of the Dorado group from the ES0-VLT Survey Telescope (VST hereafter, Schipani et al. 2012). Such images were obtained within the VEGAS-survey of nearby ETGs (Capaccioli et al. 2015; Spavone et al. 2017). The plates used reach a surface brightness of 30.5 mag arcsec⁻² in g and 29.0 mag arcsec⁻² r bands with a resolution of (0.21/px) and a total field of view of 1° × 1°. The full analysis of the optical data will be presented in a forthcoming companion paper (Ragusa et al. 2022, in preparation). We use VST images in order to compare the optical R_{g29} and R_{r28} galaxy radii at $\mu_g=29$ mag arcsec⁻² and $\mu_r=28$ mag arcsec⁻², respectively, with the distribution and the extension of the FUV.CaF2 emission.

The plan of the paper is the following. Section 2 presents target galaxies and provides the motivation of the UVIT study. In § 3 we present FUV.CaF2 observations and the reduction techniques adopted. The morphological and photometric analysis performed and determination of star formation rate (SFR) from the FUV.CaF2 integrated galaxy luminosity are detailed in § 4. The FUV.CaF2 properties of individual galaxies are presented and summarized in § 5. We discuss in § 6 the FUV.CaF2 versus optical extensions of our target galaxies. In Section 7 we discuss and compare the SFR from the FUV.CaF2 flux with the values obtained from the H α flux by Ram2020. We summarize our results and draw some conclusions in § 8.

2. The target galaxies and motivation of the FUV study

Ram2020 used H α + [N II] imaging to derive the SFR of the Dorado backbone galaxies consisting of 6 LTGs, namely IC 2038, NGC 1536, IC 2058, PGC 75125, NGC 1566, NGC 1602 and 8 ETGs, from Es to S0-a with a large fraction of S0s, namely IC 2039, NGC 1533, NGC 1543, NGC 1546, NGC 1549, NGC 1553, NGC 1581 and NGC 1586. The LTG SFR ranges from 0.01±0.001 to 2.2±0.2 M $_{\odot}$ yr⁻¹. These values suggested that LTGs in Dorado have a large spread in the SFR if compared with a general LTG sample (see e.g. James et al. 2004). The SFR of ETGs ranges from 0.008±0.003 to 1.01±0.10 M $_{\odot}$ yr⁻¹. The comparison with the ETGs sample of Gavazzi et al. (2018), suggested that the SF in Dorado ETGs are not yet shut down. Ram2020 proposed that mechanisms such as gas stripping and gas accretion, through galaxy-galaxy interaction, are relevant in this evolutionary phase of Dorado.

The measure of the SFR from H α + [N II] imaging for ETGs is challenging due to the low H α emission fluxes, that need both a careful continuum subtraction and [NII] line correction (see e.g. Gavazzi et al. 2018; Karachentsev & Kaisina 2013). This motivated us to complement the Ram2020 study probing the SFR using FUV.CaF2 (1300-1800 Å) observations obtained with ASTROSAT-UVIT of the same Dorado members. UVIT observations have been used in Ram2021 to study the South West part of the group, which includes the sub-structure composed of NGC 1533, IC 2038 and IC 2039 (see Figure 1).

This paper completes the UVIT FUV.CaF2 study of the Dorado backbone. Our targets map the Dorado central region, the SGC 0414-5559 compact group together with NGC 1536, and its North-East extension (Figure 1) dominated by the pairs NGC 1566/NGC 1581 and NGC 1596/NGC 1602. Table 1 provides some relevant properties of the galaxies here considered. All targets, except for NGC 1596 and NGC 1602, had been previously imaged in UV (FUV and NUV) with GALEX, in a broad passband similar to FUV.CaF2 as the UVIT filter used here, but at about 5 times lower resolution. Therefore, the new UVIT data are a significant improvement in resolution with respect to GALEX UV studies, as they probe the

FUV morphology on about 0.14 kpc scale, the typical size of SF complexes, and they are first FUV view of these two galaxies.

3. Observations and data reduction

Astrosat is a X-ray - UV observatory launched by the Indian Space Research Organization on September 28, 2015. The Ultra-Violet Imaging Telescope facility UVIT (Tandon et al. 2017) is composed of two Ritchey-Chretien telescopes with 37.5 cm aperture, a circular field of view of 28' diameter, originally observing simultaneously one in FUV (1300-1800 Å) and the other both in Near UV (NUV) (2000-3000 Å) and optical band, VIS (3200-5500 Å), by means of a beam-splitter directing NUV and VIS to individual cameras.

The NUV detector is currently not working. Therefore, observations have been performed with the FUV channel only. We used the full field of view, in photon counting mode, with the Filter F148W CaF2 ($\lambda_{mean}=1481$, $\Delta\lambda=500\text{\AA}$). Photons are counted on a planar CMOS array at approximately 28 Hz and stacked to reconstruct the image (see for details Postma et al. 2011; Kumar et al. 2012; Postma & Leahy 2017; Tandon et al. 2017) with the astrometric world coordinate solution solved automatically by a trigonometric algorithm (Postma & Leahy 2020).

Table 2 compiles the relevant information on the Astrosat-UVIT observations obtained in two programs A05_002 and A07_010 (PI R. Rampazzo). The first covers the three members of the compact group SGC 0414-5559, i.e. NGC 1549 (Field C), NGC 1553 (Field D) and IC 2058 (Field E). The A07_010 program observed the fourth member of the compact group NGC 1546 (Field B) and NGC 1536 (Field A), located South of the NGC 1533 sub-structure (see Ram2020). NGC 1536 has a recession velocity similar to that of the compact group. Observations of NGC 1566 (Field F) have been obtained from the ASTROSAT archive (program G06_087 PI S. Stalin). We used only the FUV.CaF2 observation for consistency with our programs.

4. Data Analysis

Images reconstructed from the photon-counting data with $0''.416$ subsampling have been rebinned for our analysis, to enhance S/N, to $1''.664 \text{ px}^{-1}$. The nominal zero point magnitude of the FUV.CaF2 filter is 18.08 mag (Tandon et al. 2017).

Surface photometry has been performed using ELLIPSE fitting routine in the STSDAS package of IRAF (Jedrzejewski 1987), increasing the size of the apertures logarithmically. Foreground and background objects have been masked. The present UVIT FUV.CaF2 observations allow to measure surface brightness profiles down to $\mu_{FUV} \sim 29 - 30 \text{ mag arcsec}^{-2}$ with an error of $\pm 0.3-0.5 \text{ mag arcsec}^{-2}$.

We applied the procedure outlined by Ebeling et al. (2006), ASMOOTH, to enhance the signal-to-noise (S/N) ratio in the galaxy outskirts, in order to bring out faint structures in the UV image. The only parameter required by the procedure is the minimum S/N, τ_{min} . The algorithm increases the smoothing scale until the S/N within the kernel reaches the τ_{min} input value. ASMOOTH suppresses very efficiently the noise while the signal, locally significant at the selected S/N level, is preserved on all scales.

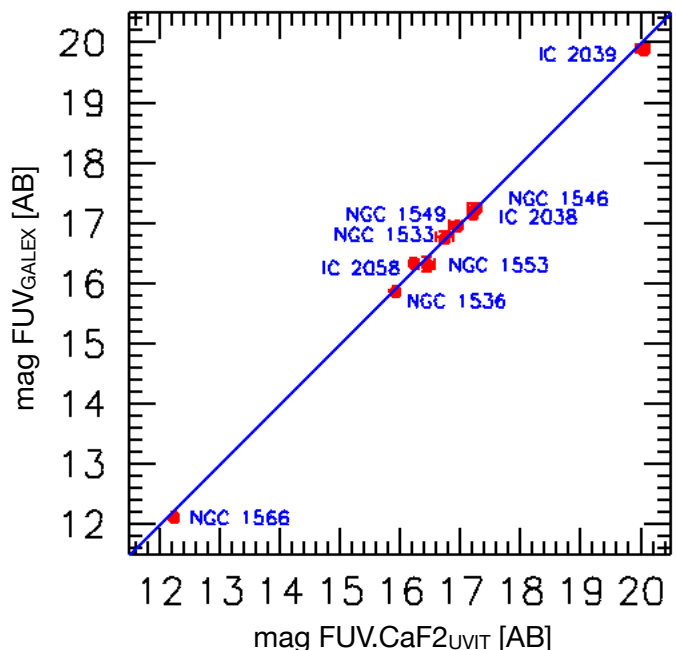


Fig. 2. Comparison with FUV GALEX magnitudes reported in Table 1. The comparison includes galaxies in Ram2021, namely NGC 1533, IC 2038 and IC 2039, whose magnitudes are corrected for foreground Galactic extinction as described in their Table 3.

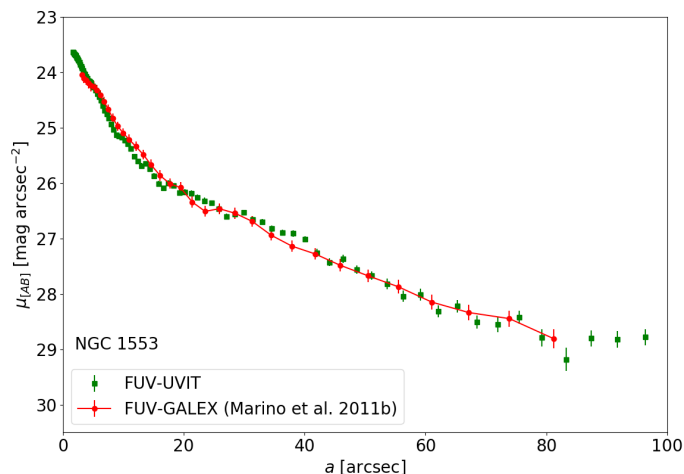


Fig. 3. UVIT FUV.CaF2 luminosity profile of NGC 1553 (green squares) compared with that of Marino et al. (2011b) from FUV-GALEX observations. The UVIT image of NGC 1553 was binned 4×4 ppx.

4.1. Integrated magnitudes and surface photometry

We derived apparent magnitudes by integrating the surface brightness within elliptical isophotes. The ELLIPSE task defines the elliptical contours of the isophotes and accounts for the geometrical information contained in the isophotes allowing the variation of the ellipticity, $\epsilon = 1 - b/a$, and position angle, PA , along the ellipse major axis, a . The task provides also a measure of the isophotal shape parameter, the so-called a_4 parameter from the fourth cosine component of the Fourier analysis of the fitted ellipse, allowing to distinguish between boxy ($a_4 < 0$) and disk ($a_4 > 0$) isophotes (Bender et al. 1988). ELLIPSE, widely applied to optical images of ETGs, has been used by Jeong et al. (2009) and Marino et al. (2011b) in order to obtain the surface photometry of ETGs from GALEX FUV data. Since irregular and peculiar features, such as clumps expected in FUV images,

Table 2. UVIT observations

Field ID	Obs ID	Observing date	Exp. Time [s]	Target ID
A	A07 3238	October 16, 2019	6627.635	NGC 1536
B	A07 3240	October 16, 2019	6669.294	NGC 1546
C	A05 2460	October 26, 2018	3311.534	NGC 1549
D	A05 2460	October 27, 2018	3354.349	NGC 1553
E	A05 2458	October 26, 2018	3189.382	IC 2058
F	G06_87	December 26, 2016	2940.386	NGC 1566
G	A07 3582	March 21, 2020	2819.043	NGC 1596

Notes. Field identification in **Col. 1** refers to the programs A05_02 and A07_010 (PI. R. Rampazzo) listed in Col. 2. In Col. 3 and Col. 4 we report the observing date and the total effective exposure time. Col. 5 gives the central target.

induce sudden variations in both ϵ and PA we notice that the isophotal shape parameter, a_4 , loses its physical meaning. For this reason in Table 3, which collects the relevant parameters derived by our FUV.CaF2 surface photometry we provide only the average ellipticity $\langle\epsilon\rangle$ and position angle $\langle P.A.\rangle$ (columns 4 and 5 respectively).

We estimated magnitude uncertainty by propagating the statistical errors on the isophotal intensity. Table 3 (col.3) provides the FUV CaF2-1, UVIT integrated magnitudes, corrected for Galactic foreground extinction as in Ram2021. The comparison with the current literature (Table 1) is shown in Figure 2 and discussed in Section 5.

FUV.CaF2 images are shown in the top left panel of Figures 4, 5, 6, 7, 8, 9, 10, and 11. Irregular and peculiar features are shown by NGC 1536, PGC 75125, IC 2058 and CMI[2001]4136-01. Spiral arms are visible in NGC 1546 and NGC 1566.

The UV surface photometry of NGC 1553 has been investigated by Marino et al. (2011b) with GALEX. Figure 3 compares our UVIT luminosity profile with that of Marino et al. (2011b). Profiles are consistent. GALEX FUV PSF FWHM is $4.2''$ (Morrissey et al. 2007) with respect to the nominal value of $1''.5$ of UVIT (Tandon et al. 2017). We check our PSF using the star TYC 8505-1906-1, a single star in the Tycho II stellar catalogue, located in the UVIT field D, which includes NGC 1553. We fit the stellar profile with a 2D single Gaussian. The best fit provides a $FWHM_{RA}=1''.68$ and $FWHM_{Dec}=1''.47$, i.e. the stellar image has an ellipticity of 0.13. Therefore, the FWHM value is consistent with nominal value measured by Tandon et al. (2017).

4.1.1. UVIT FUV.CaF2 versus GALEX FUV magnitudes

In Figure 2 we compare our UVIT FUV.CaF2 asymptotic magnitudes, obtained integrating the galaxy luminosity profiles (see Section 4.1) with FUV GALEX asymptotic magnitudes reported in Table 1. The comparison includes Dorado members located in the NGC 1533 sub-structure, obtained in the same way by Ram2021. UVIT FUV.CaF2 agree with GALEX FUV magnitudes, as expected given that the two filters have somewhat similar bandpasses.

4.1.2. Analysis of the FUV-CaF2-1 surface brightness profiles

We fit the azimuthal FUV-CaF2-1 surface brightness profiles of galaxies with a single Sérsic law (Sérsic 1963). We are aware that in some case it represents a crude representation of the sur-

face brightness profile. However, a simple Sérsic law, provides useful information that can be compared with existing results for larger samples. The Sérsic law $\mu \propto a^{1/n}$, where μ is the surface brightness, a the semi-major axis and n the Sérsic index, is a generalization of the de Vaucouleurs et al. (1992) $a^{1/4}$ and Freeman (1970) exponential laws. The value of n accounts for the variety of the shapes of the surface brightness profiles of ETGs with $n = 4$ representing the ‘classic’ Elliptical’s shape. An exponential disc (Freeman 1970) has an index $n = 1$. UV surface brightness profiles of ETGs may reach large values of n (see e.g. Marino et al. 2011b). Rampazzo et al. (2017), by comparing UV and optical data from Swift-UVOT of eleven EGTs, suggested that, if $n < 3$, the presence of a disk starts to emerge. The value $n < 2.5$ is also adopted in optical surveys to isolate disk galaxies (see e.g. Meert et al. 2015).

The Sérsic law fit is shown in the top right panels of Figures 4, 5, 6, 7, 9, 10 and 11, superposed to the UVIT FUV.CaF2 surface brightness profiles. The fit, that accounts for the UVIT-PSF, is extended to the whole profile up to the background. We did not mask FUV bright sub-structures such as the bar in NGC 1536 and the knots in IC2058 or NGC 1602. The values of the Sérsic index obtained from the fits are collected in column 6 of Table 3.

4.2. The recent Star Formation Rate from FUV.CaF2 integrated galaxy luminosity

Both $H\alpha$ and FUV luminosities trace recent SF, although they map slightly different age ranges. Kennicutt & Evans (2012, their Table 1) indicated an age range of 0–100 Myr and of 0–10 Myr for the stellar populations contributing to FUV and $H\alpha$, with a mean ages of 10 and 3 Myr, respectively, although the age strongly depends on stellar metallicity (Bianchi 2011, their Figure 5).

From the integrated FUV luminosity of Dorado members we derived their recent SFR, following Lee et al. (2009, their equation 3):

$$SFR[M_{\odot} \text{ yr}^{-1}] = 1.4 \times 10^{-28} L_{FUV}[\text{erg s}^{-1} \text{ Hz}^{-1}] \quad (1)$$

Results are given in column 8 of Table 3. The Galactic extinction correction is $A_{FUV}=7.9 \times E(B-V)$ (Lee et al. 2009, see also Ram2021) using the $E(B-V)$ values provided by Ram2020 in Table 3. No internal dust attenuation has been applied.

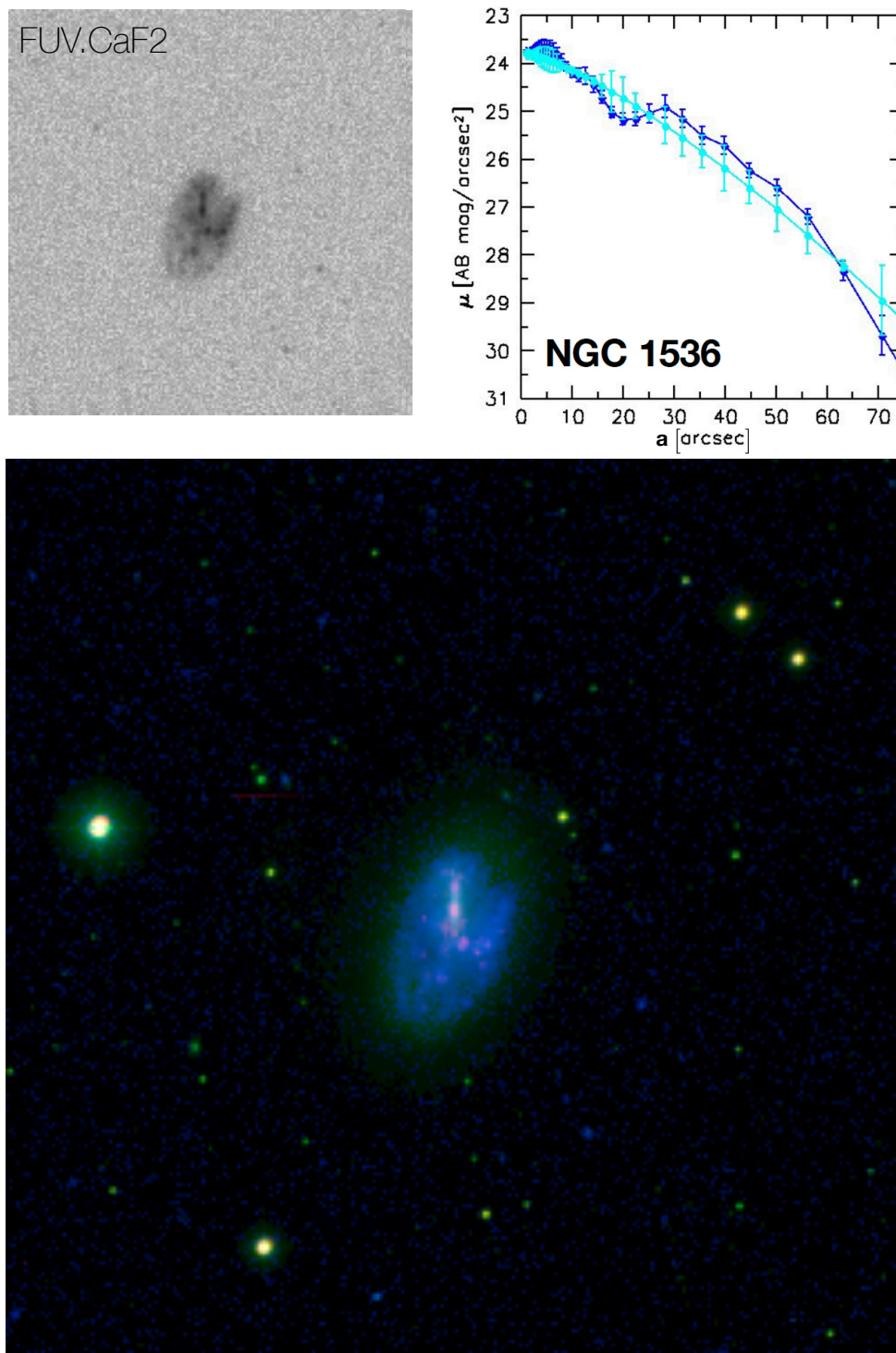


Fig. 4. (*Top left panel*) UVIT FUV.CaF2 image of NGC 1536. The image size is $7' \times 7'$. North is on the top and East to the left. (*Top right panel*) UVIT FUV.CaF2 surface brightness profile (blue). The single Sérsic law fit is superposed (cyan) the light profile. (*Bottom panel*) Colour composite RGB image of NGC 1536 using $H\alpha+[N II]$ and nearby continuum images (from Ram2020) as red and green channels and FUV.CaF2 image as blue channel. Both the $H\alpha+[N II]$ and the continuum images have been re-sampled to the UVIT image resolution.

5. Results

5.1. Individual Notes

Table 3 presents results derived from our FUV.CaF2 analysis, including luminosity scaled to the distance of 17.69 Mpc. In the following we discuss the results in terms of the galaxy type classification, which is revised here based on the FUV.CaF2 morphology and the Sérsic index.

NGC 1536 The FUV.CaF2 image (Figure 4, top left panel) shows the irregular arm structure of this barred spiral galaxy (SBc, according to HyperLeda). We can clearly see its off-centered bar. The average FUV.CaF2 $\langle PA \rangle = 162^\circ$ is consistent with the optical one at R_{25} (Table 1). The average ellipticity,

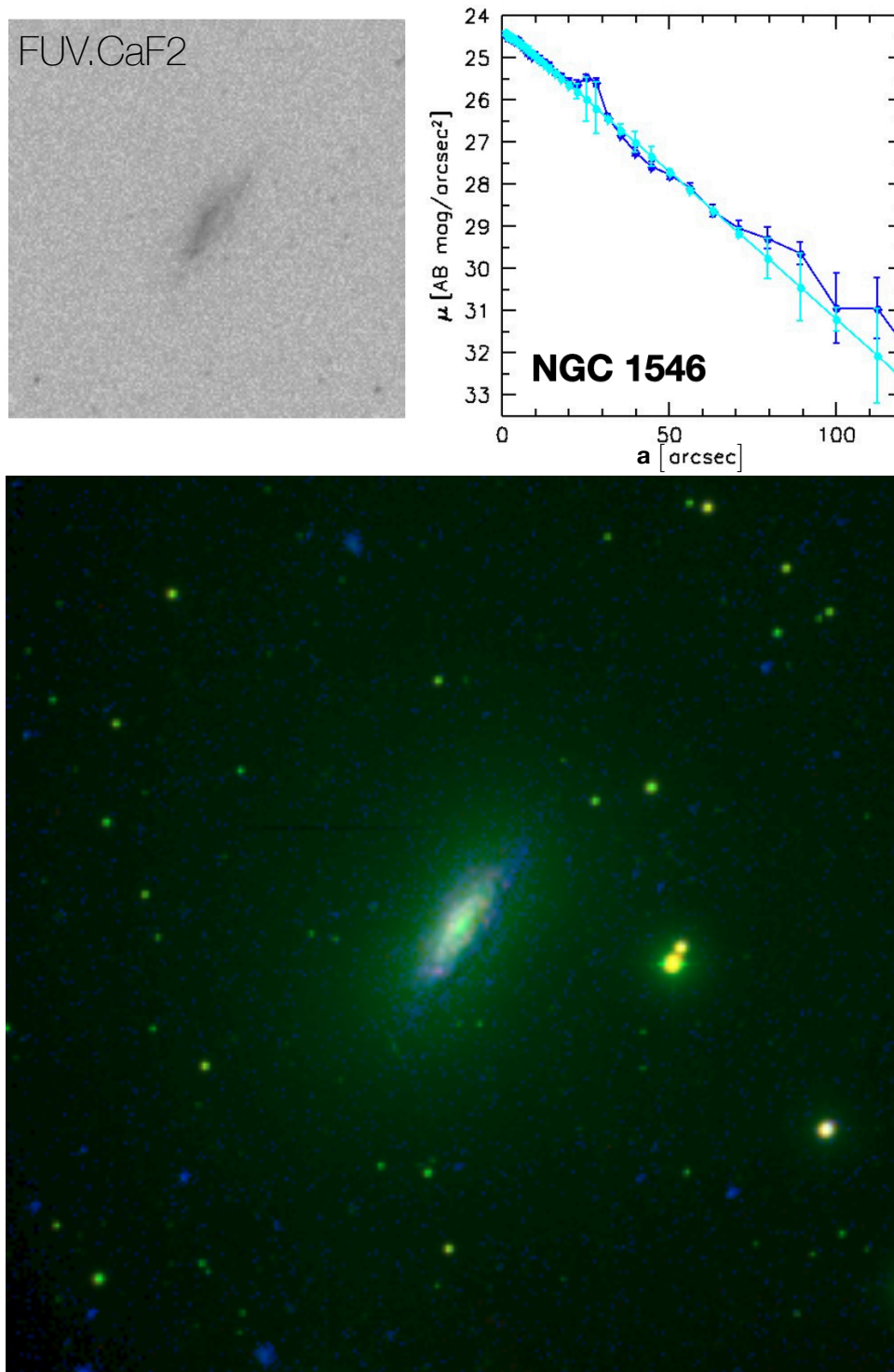


Fig. 5. As in Figure 4 for NGC 1546. The image size is $7' \times 7'$. North is on the top and East to the left.

$\langle \epsilon \rangle = 0.40$ (Table 3), differs from the optical one, 0.28 (Table 1) due to ellipticity variations of the FUV.CaF2 emission.

The index obtained from the Sersic law fit, $n = 0.76 \pm 0.02$, suggests the presence of a disk. The H II regions found by Ram2020 stand out in red in Figure 4. They are distributed along the brightest features of the FUV.CaF2 emission (bar and arm segments), although the FUV.CaF2 emission is more diffuse and extended (see also Section 6).

At $30 \text{ mag arcsec}^{-2}$ the FUV.CaF2 luminosity profiles extends up to $70''$ well outside $49'' \cdot 8$, the R_{25} isophote in the B-

band. Notice, however, the larger extension of the R-band continuum (green) with respect to FUV.CaF2 emission (blue) in the bottom panel of Figure 4.

NGC 1546 This galaxy (Figure 5) has an uncertain classification. Comerón et al. (2014) classified it as E(b)3/(R')SA(r)ab, i.e. it could be either an ETG, as suggested by HyperLeda that reports a classification of S0-a, or a spiral with an inner ring (r) and an outer pseudo-ring (R'). The FUV.CaF2 image (top left panel) shows diffuse emission in the outer regions and the colour-composite image (bottom panel) reveals a spiral structure

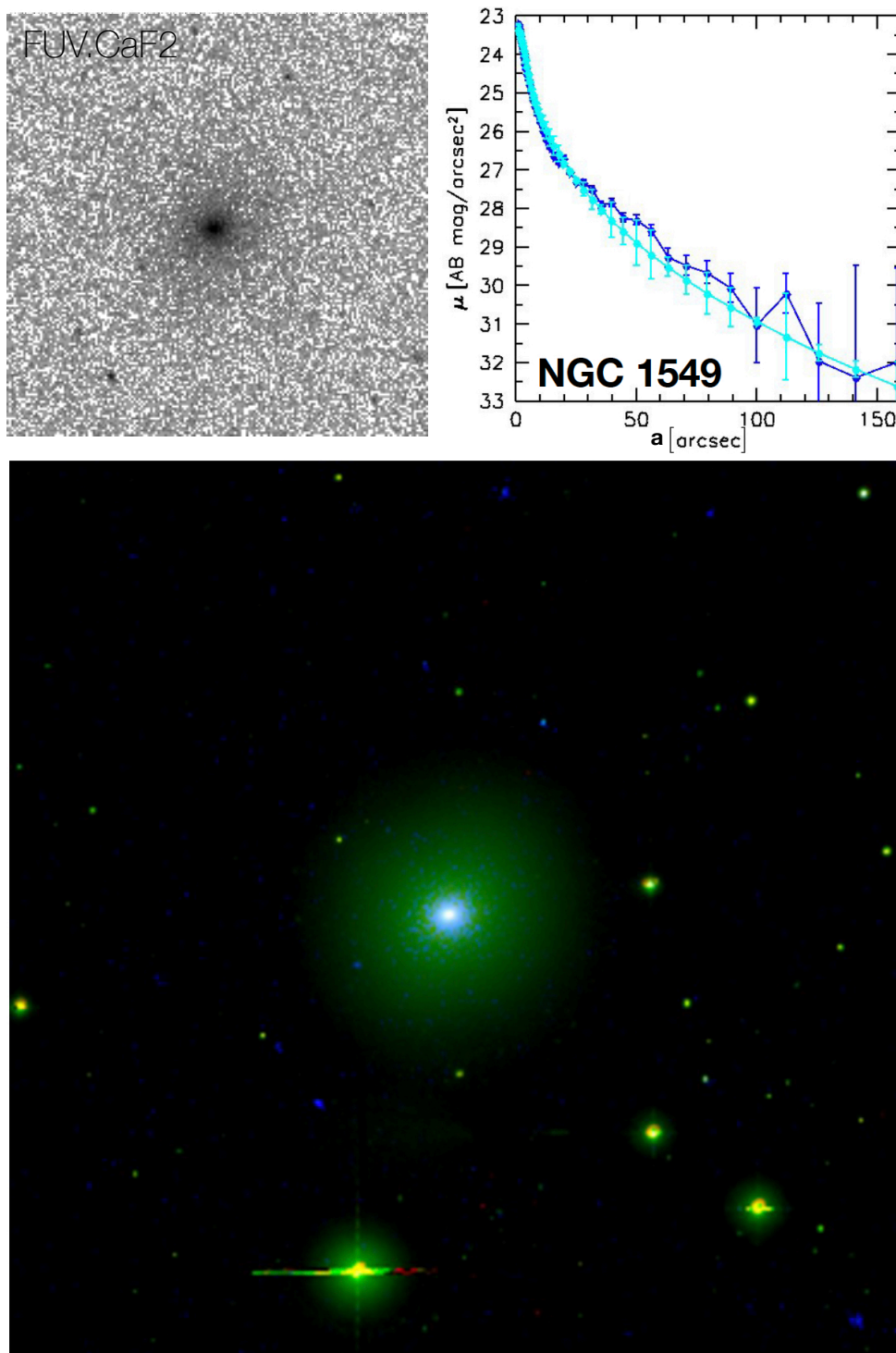


Fig. 6. As in Figure 4 for NGC 1549. The image size is $8' \times 8'$. North is on the top and East to the left.

embedded in a diffuse halo. However, the shape of this galaxy is reminiscent of 3D ETGs mentioned by Buta et al. (2015), in the R continuum and $H\alpha + [N II]$ bands. The FUV.CaF2 average position angle is consistent with the optical, 144.8° , at R_{25} from HyperLeda and $152.4^\circ \pm 0.7$ from the Carnegie Galaxy Survey (CGS hereafter) in the I band (Ho et al. 2011). The average FUV.CaF2 ellipticity, $\langle \epsilon \rangle = 0.66$, is twice as large as the optical one (Table 1).

The fit of the surface brightness profile with a Sérsic index $n = 0.98 \pm 0.04$ is shown in top right panel of Figure 5. The FUV.CaF2 structure results basically a disk with a bump that

peaks at about $26''$ or 2.6 kpc. Comerón et al. (2014) find an inner closed ring (r) and an outer pseudo-ring (R') in this galaxy. The bump we detect in FUV.CaF2 corresponds to the R' pseudo-ring, that Comerón et al. (2014) detect at $a=28''$.

NGC 1549 The FUV.CaF2 image of this galaxy, shown in Figure 6, contrasts with the large scale optical system of shells and plumes discovered by (Malin & Carter 1983). These features, due to old stellar populations, are not detected in our red continuum image (Figure 6, green in the composite image) since the short exposure time (see also the CGS study by Ho et al.

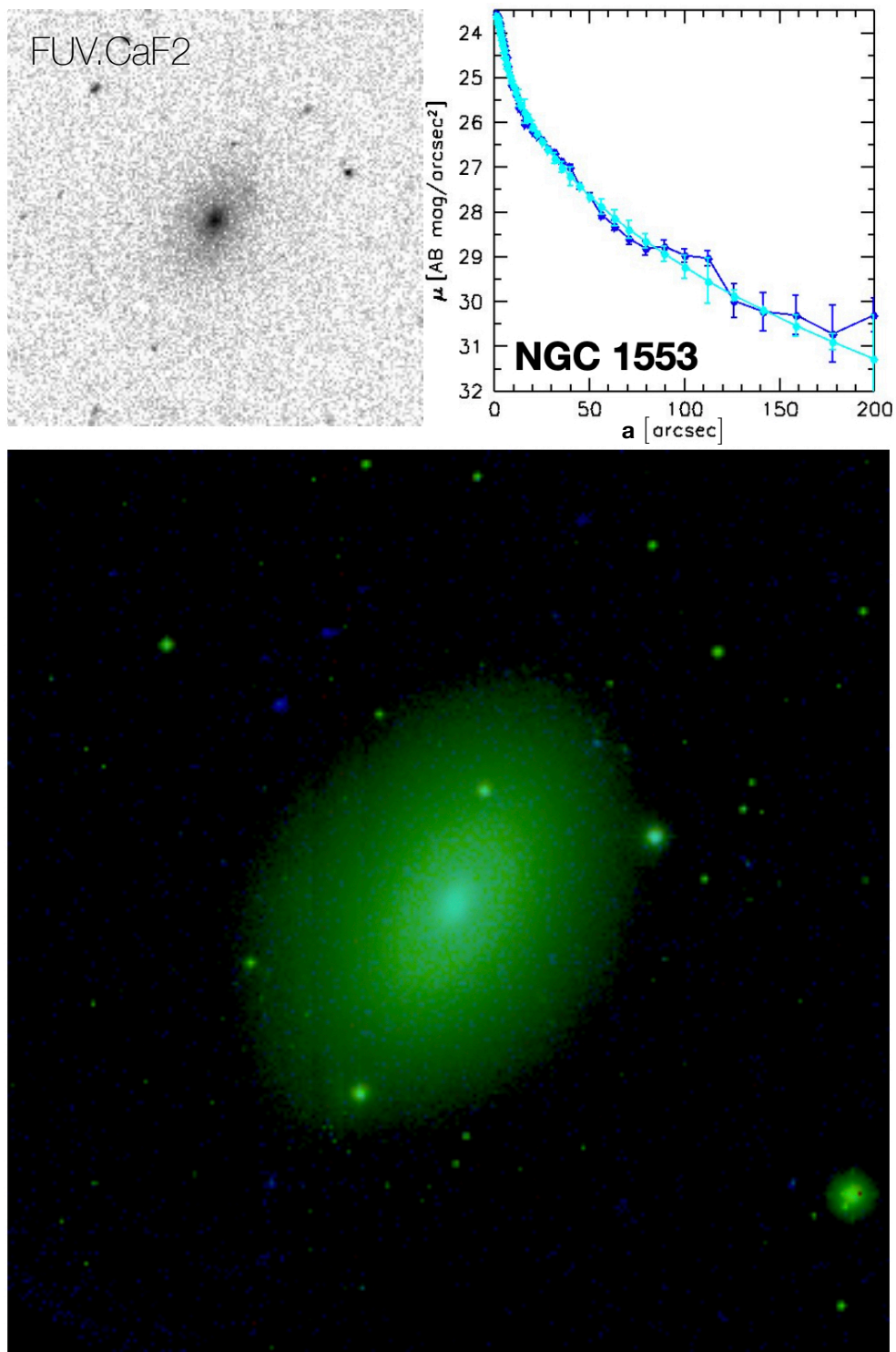


Fig. 7. As in Figure 4 for NGC 1553. The image size is $7' \times 7'$. North is on the top and East to the left.

(2011)). The colour-composite image evidences a blue ring in the inner part (≈ 10 - $20''$ radius) as revealed from our FUV.CaF2 luminosity profile but not from optical data (Ho et al. 2011) and $H\alpha$ by Ram2020.

The average ellipticity, $\langle \epsilon \rangle = 0.07$, and position angle, $\langle PA \rangle = 0^\circ$ account for the roundness and smoothness of the FUV.CaF2 emission unlike the B-band optical evaluation of HyperLeda which provides $\epsilon = 0.15$ and $PA = 146.2^\circ$ at R_{25} . The PA of I-band image of CGS (Ho et al. 2011) $173.8^\circ \pm 2.7$ is consistent with the FUV.CaF2 measure.

Our Sérsic fit of the surface brightness profile gives an index $n = 2.86 \pm 0.28$ suggesting that, in the FUV.CaF2 band, NGC 1549 is a E/S0.

NGC 1553 The HyperLEDA classification for this galaxy is S0 with a ring. Malin & Carter (1983) discovered a wide system of shells around this galaxy (see their Figure 2). The colour-composite image shown in Figure 7 does not show such features, neither in FUV.CaF2, as expected, nor in the red continuum image due to the short exposure times.

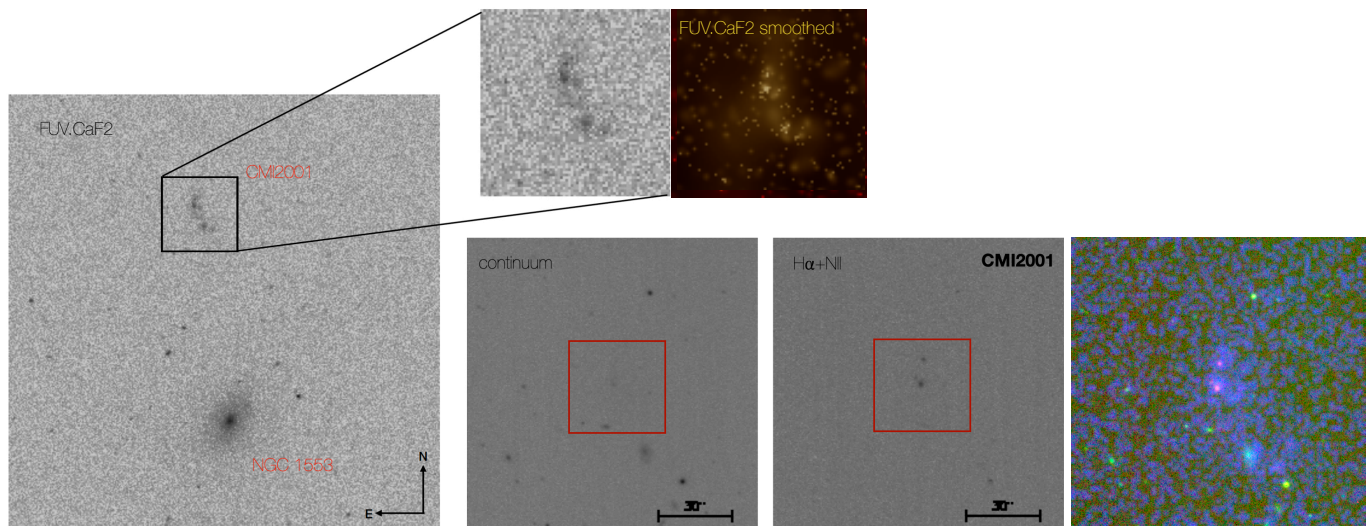


Fig. 8. (Left panel) UVIT FUV.CaF2 image of CMI2001 in the field of NGC 1553. The size of the figure is $7' \times 7'$. (Top panels) Zoom on [CMI2001]4136-01 FUV.CaF2 region, $2' \times 2'$ wide, before and after smoothing with ASM00TH and $\tau_{min}=1.5$. (Bottom panels) [CMI2001]4136-01 image in continuum and $H\alpha+[N II]$ adapted from Ram2020. The red square encloses the CMI2001 region. The bottom right panel shows the RGB colour-composite image obtained from the continuum, $H\alpha+[N II]$, and FUV images used as the green, red and blue channels, respectively.

The recent classification by Comerón et al. (2014) suggests the presence of resonance rings in this lenticular SA(r1, nr'1)0⁺. In more detail, they found an inner close ring-lens (r1) with semi-major axis of $35''.4$, and a nuclear pseudoring-lens structure (nr'1) with semi-major axis of $9''$ (see also Ho et al. 2011). Although these features are derived by IR data, a faint bump appears in the FUV.CaF2 luminosity profile of Figure 7 between $30-40''$, corresponding to the ring-lens (r1) above. $H\alpha$ emission has been detected by Fabry-Perot (FP) high resolution observations of the NGC 1553 inner regions (Rampazzo et al. 2007). The FP $H\alpha$ monochromatic map in the inner $30''$ results quite clumpy (see Figure 8 in Ram2020).

The average FUV.CaF2 PA and ellipticity are very similar to the optical values at R_{25} , that are $PA=150.4^\circ$ and $\epsilon=0.31$, respectively. PA of $151.3^\circ \pm 1.5^\circ$ is measured in the I-band by CGS (Ho et al. 2011).

The right panel of Figure 7 shows the Sérsic fit of the surface brightness profile. The Sérsic index obtained, $n = 2.67 \pm 0.21$, is consistent with that derived by Marino et al. (2011b) with the same method using GALEX FUV observations. This value suggests that FUV.CaF2 emission is structured in a disk, i.e. the galaxy is a E/S0 consistently with the HyperLeda morphological type in Table 1.

[CMI2001]4136-01 This source, detected by Ram2020 (their Figures 9 and 10) in $H\alpha+[N II]$, probing its association to the Dorado group, reveals a complex and irregular morphology in our colour-composite image (Figure 8). This source has been classified as a galaxy in the GALEX-database.

The bottom panel of Figure 8 shows $H II$ regions within the faint structure of [CMI2001]4136-01. The case may be reminiscent of $H II$ regions found by Werk et al. (2010) in the very periphery of NGC 1553, in the Noth East sub-structure of Dorado. These seem connected with ongoing interaction between NGC 1553 and IC 2038/IC 2039 suggested in optical by Cattapan et al. (2019), in $H I$ by Ryan-Weber et al. (2003, 2004) and Kilborn et al. (2009) and in FUV.CaF2 by Ram2021. In this context, [CMI2001]4136-01, projecting on an optical shell of NGC 1553 (see also Figure 2 in Malin & Carter (1983)), could be distorted by the interaction with the Dorado centre (SCG0414-5559), a

region that, at odds with NGC 1553, is $H I$ poor (Elagali et al. 2019).

IC 2058 and PGC 75125 IC 2058 and PGC 75125 are part of the Dorado central compact group SCG 0414 -5559 (Iovino 2002). A distortion of PGC 75125 is evident from the FUV.CaF2 image (Figure 9). The two galaxies, separated by $\Delta V_{hel} = 28 \text{ km s}^{-1}$, are likely interacting, as suggested by both the shape of the present FUV.CaF2 emission and $H I$ observations by Elagali et al. (2019, their Figure 14).

The FUV.CaF2 image of IC 2058, seen edge-on, does not show distortions. The smoothed image, shown in the bottom right panel of Figure 9, shows the presence of some extra-planar features, not detected in $H\alpha$ both by (Rossa & Dettmar 2003) and Ram2020.

The geometrical parameters of IC 2058, $PA=17.9^\circ$ and $\epsilon=0.85$, at R_{25} in Table 1 are very similar to the average $\langle \epsilon \rangle = 0.74$ and $\langle PA \rangle = 18^\circ$ obtained from the FUV.CaF2 surface photometry (Table 3).

The single Sérsic law fits of both galaxies luminosity profiles, shown in the top central and right panels of Figure 9, with index $n = 1.48 \pm 0.10$ for IC 2058 and $n = 1.20 \pm 0.03$ for PGC 75125 trace the presence of a disk in both these galaxies (Table 3).

NGC 1566 The FUV.CaF2 emission (Figure 10) of this grand design spiral, classified by Comerón et al. (2014) (R')SAB(r'l,s,nb)b, is very extended with the outermost spiral arm out to about $6'.7$ (about 31 kpc). This radius is larger than both the optical B-band radius at μ_{25} , $3'.62$ (HyperLeda), and the I-band emission radius measured at 26.5 mag arcsec⁻² that reaches $4'.06$ (Ho et al. 2011) (see Section 6 and Table 4.)

The optical position angle and ellipticity measured at R_{25} , $PA=44.2^\circ$ and $\epsilon=0.32$, differ from those provided by the FUV.CaF2 surface photometry. FUV.CaF2 isophotes appear nearly round with average ellipticity 0.05 and position angle 15° . The PA measured in the I-band by CGS is $26.4^\circ \pm 4.7^\circ$.

In the top right panel of Figure 10 are shown our surface brightness profile and single Sérsic law fit. The fit does not interpret the inner ring. The Sérsic index, $n = 0.94 \pm 0.05$, follows the

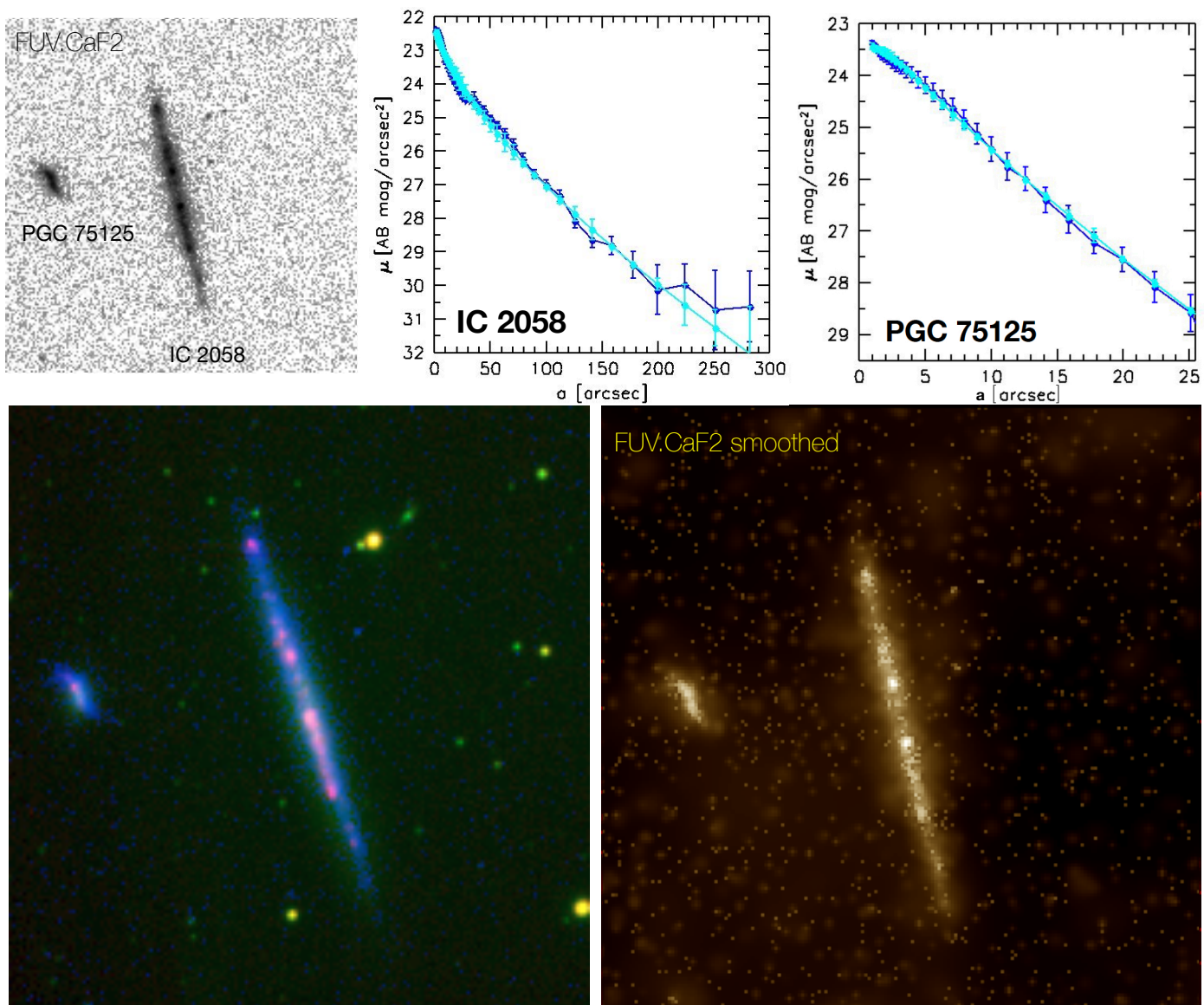


Fig. 9. (Top left panel) UVIT FUV.CaF2 image of IC 2058 and PGC 75125 at the centre of the frame and at the East side, respectively. The image size is $5' \times 5'$. North is on the top and East to the left. (Top central panel) FUV.CaF2 surface brightness profile (blue) of IC 2058 and (top right panel) of PGC 75125. Single Sérsic law is superposed (cyan), to fit the light profile. (Bottom left panel) Colour-composite RGB image of IC 2058 and PGC 75125 as in Figure 4. (Bottom right panel) FUV.CaF2 image smoothed using the `ASMOOTH` task with $\tau_{min}=1.5$.

general disk structure, while the actual profile shows deviations corresponding to the spiral arms.

NGC 1596 and NGC 1602

Our UVIT image is the first UV view of both these systems. Our composite image (Figure 11) shows that the FUV.CaF2 emission dominates the light of the irregular galaxy NGC 1602 whereas it is mixed to older stellar populations in NGC 1596. We enhanced the signal of faint structures using `ASMOOTH` task to look for a FUV connection between the two galaxies following the behaviour the $H\alpha$ emission (Bureau & Chung 2006; Elagali et al. 2019) without success.

The smoothed image (bottom right panel), however, reveals extra-planar light, so the FUV disk loses the regular shape shown in the optical bands (bottom left panel).

The value of the Sérsic index in Figure 11 (top: central and left panels) $n = 2.12 \pm 0.18$ (Table 3) is consistent with the presence of a disk in NGC 1596. The average position angle and el-

lipticity, 0.5 and 20° , are consistent with HyperLeda values (Table 1) and the I-band measure of the PA $20.0^\circ \pm 0.8^\circ$ from CGS.

The surface brightness profile of NGC 1602 is very irregular as the shape of the galaxy which is classified a SBm in optical. The average ellipticity and position angle, 0.3 and 80° are consistent with HyperLeda values (Table 1).

The Sérsic index, $n = 0.25 \pm 0.04$, results from the irregular shape of the FUV.CaF2 light distribution in this galaxy. Notice that the case $n = 0.5$ corresponds to a Gaussian.

We summarize the results of our FUV.CaF2 morphological and structural analysis.

- All surface brightness profiles are fitted by a 1D single Sérsic law with $n < 3$ suggesting that the FUV.CaF2 structure of

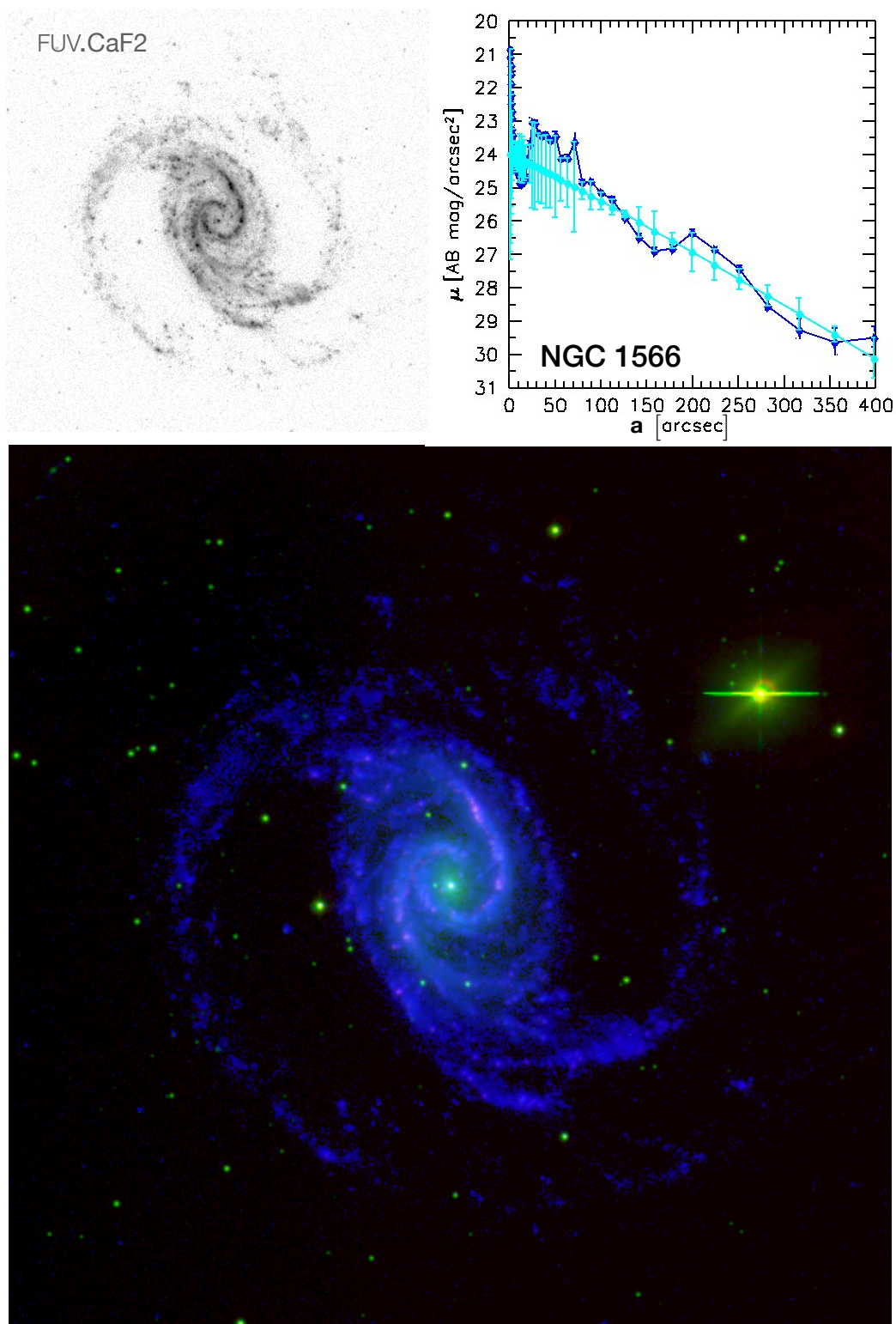


Fig. 10. As in Figure 4 for NGC 1566. The image size is $13' \times 13'$. North is on the top and East to the left.

most of the Dorado members we analysed, including ETGs, has a disk shape. Such FUV structures have been formed via dissipative mechanisms (Rampazzo et al. 2017).

- NGC 1536 shows an off-centred bar. FUV.CaF2 rings are frequently detected both among ETGs and LTGs. Our findings support previous GALEX observations, (Jeong et al. 2009; Marino et al. 2011a,b) showing that these rings are SF sites (Bianchi 2011), associated to H II regions, as for NGC

1546, NGC 1566, NGC 1581 (Ram2020) and NGC 1533 (Ram2021).

- We observe FUV.CaF2 extra-planar emission from the disk of IC2058 and NGC 1596. (Figure 9 and Figure 11, right bottom panels). We fail in revealing FUV.CaF2 diffuse emission in correspondence to H I emission in between IC 2058/PGC 75125 and NGC 1596/NGC 1602 (Chung et al. 2006; Elagali

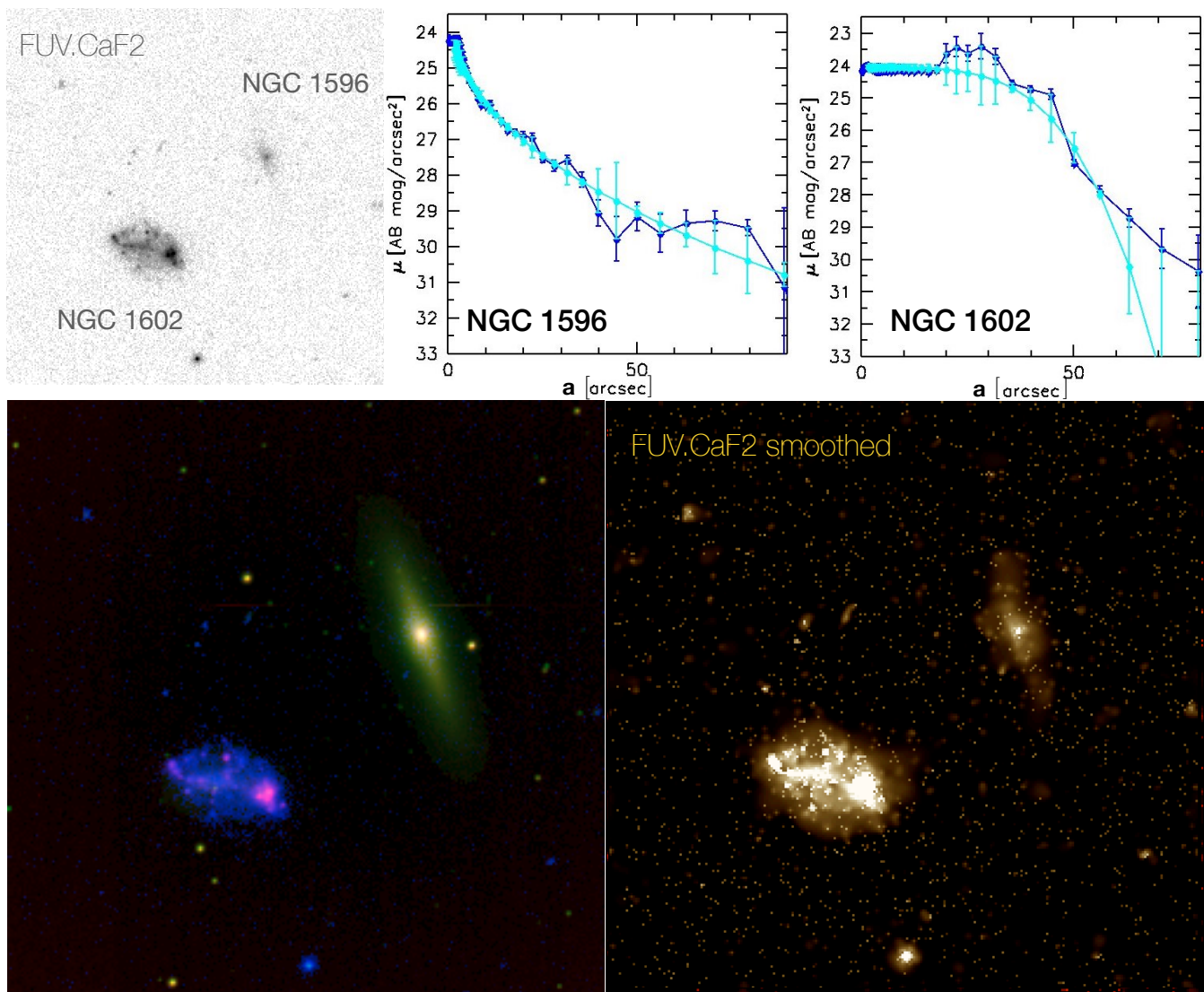


Fig. 11. (Top left panel) UVIT FUV.CaF2 image of NGC 1596 (North-west) and NGC 1602 (South-East). The image size is $7' \times 7'$. North is on the top and East to the left. (Top right panels) FUV.CaF2 surface brightness profiles of NGC 1596 and NGC 1602 (blue solid lines). The fit of a single Sérsic law is overlaid to the luminosity profile (cyan squares). (Bottom left panel) Colour composite RGB image of NGC 1596 and NGC 1602 as in Figure 4. (Bottom right panel) FUV.CaF2 image smoothed using ASMOOTH task, with $\tau_{min}=1.5$.

et al. 2019). Further insights on this point coming from deep optical images are discussed in the next section.

- Asymmetries are visible in NGC 1536, PGC 75125, NGC 1566 and CMI[2001]4136-01 likely due to tidal perturbations.

6. FUV.CaF2 versus deep optical imaging: looking for XUV emission

We intend to test the presence of XUV disks in the Dorado members, i.e. the presence of FUV emission at large galactocentric distances, up to several optical radii. Roughly 30% of spiral galaxies in the Local Universe show XUV features (Thilker et al. 2007; Gil de Paz et al. 2008; Thilker et al. 2010). This phenomenon is relevant for understanding how FUV observations intercept faint SF levels (see e.g. Bigiel et al. 2010). For comparison, we consider also the FUV.CaF2 extension versus optical in ETGs.

The FUV-optical comparison performed in Section 5, made on the basis of continuum observations from the $H\alpha+[N II]$

data-set of Ram2020, is hampered by the short exposure time through the narrow band optical filters used. In this section we compare the FUV.CaF2 extension of our targets with optical radius at 29 and 28 mag arcsec⁻² in g and r bands, respectively, as results from the deep photometry by Ragusa et al. (2022, in preparation). Table 4 reports the above values together with the $R_{26.5}$ radius in I-band measured by Ho et al. (2011).

6.0.1. The Dorado core

The left panel of Figure 12 shows a VST colour composite image of the compact group. The image includes NGC 1546, NGC 1549, NGC 1553 and IC 2058, observed with UVIT FUV.CaF2 fields B, C, D, E (see Table 1 and Figure 1). The VST images include also PGC 75125 and of [CMI2001]4136-01 projected between NGC 1549 and NGC 1553. An unsharp masking of the same field, in the g -band, is shown in the right panel. We notice that NGC 1546, in addition to NGC 1549 and NGC 1553 (Malin & Carter 1983), shows a faint shell/ripple in its South-East side. Shells are mostly revealed in ETGs while they are very rare, if

Table 3. Integrated magnitudes of Dorado in UVIT FUV.CaF2.

Field	ID source	FUV.CaF2 AB [mag]	$\langle\epsilon\rangle$	$\langle PA\rangle$ [deg]	n	$L_{FUV,CaF2}$ 10^{26} [erg s $^{-1}$ Hz $^{-1}$]	SFR [M $_{\odot}$ yr $^{-1}$]
A	NGC 1536	15.90 \pm 0.02	0.40	160	0.76 \pm 0.02	5.95 \pm 0.05	0.083 \pm 0.001
B	NGC 1546	17.24 \pm 0.11	0.66	141	0.98 \pm 0.04	1.74 \pm 0.08	0.024 \pm 0.001
C	NGC1549	16.92 \pm 0.11	0.07	0	2.86 \pm 0.28	2.32 \pm 0.01	0.033 \pm 0.001
	[CMI2001]4136-01	19.13 \pm 0.34	0.30 \pm 0.04	0.004 \pm 0.001
D	NGC 1553	16.44 \pm 0.13	0.36	150	2.67 \pm 0.21	3.63 \pm 0.20	0.051 \pm 0.003
E	IC 2058	16.22 \pm 0.04	0.74	18	1.48 \pm 0.10	4.43 \pm 0.07	0.062 \pm 0.001
	PGC 075125	18.07 \pm 0.10	0.36	20	1.20 \pm 0.03	0.81 \pm 0.03	0.011 \pm 0.0005
F	NGC 1566	12.13 \pm 0.03	0.05	15	0.94 \pm 0.05	175.30 \pm 1.93	2.455 \pm 0.027
G	NGC 1596	17.96 \pm 0.21	0.52	20	2.12 \pm 0.18	0.95 \pm 0.08	0.013 \pm 0.001
	NGC 1602	15.06 \pm 0.04	0.32	80	0.25 \pm 0.04	12.94 \pm 0.21	0.181 \pm 0.003

Notes. Col. 2 gives the galaxy identification; Col. 3 gives the extinction corrected FUV integrated magnitude; Col. 4 gives the average ellipticity; Col. 5 gives the average Position Angle; Col. 6 gives the Sersic index; Col. 7 gives the total absolute FUV luminosity; col. 8. gives the SFR as derived from eq.1.

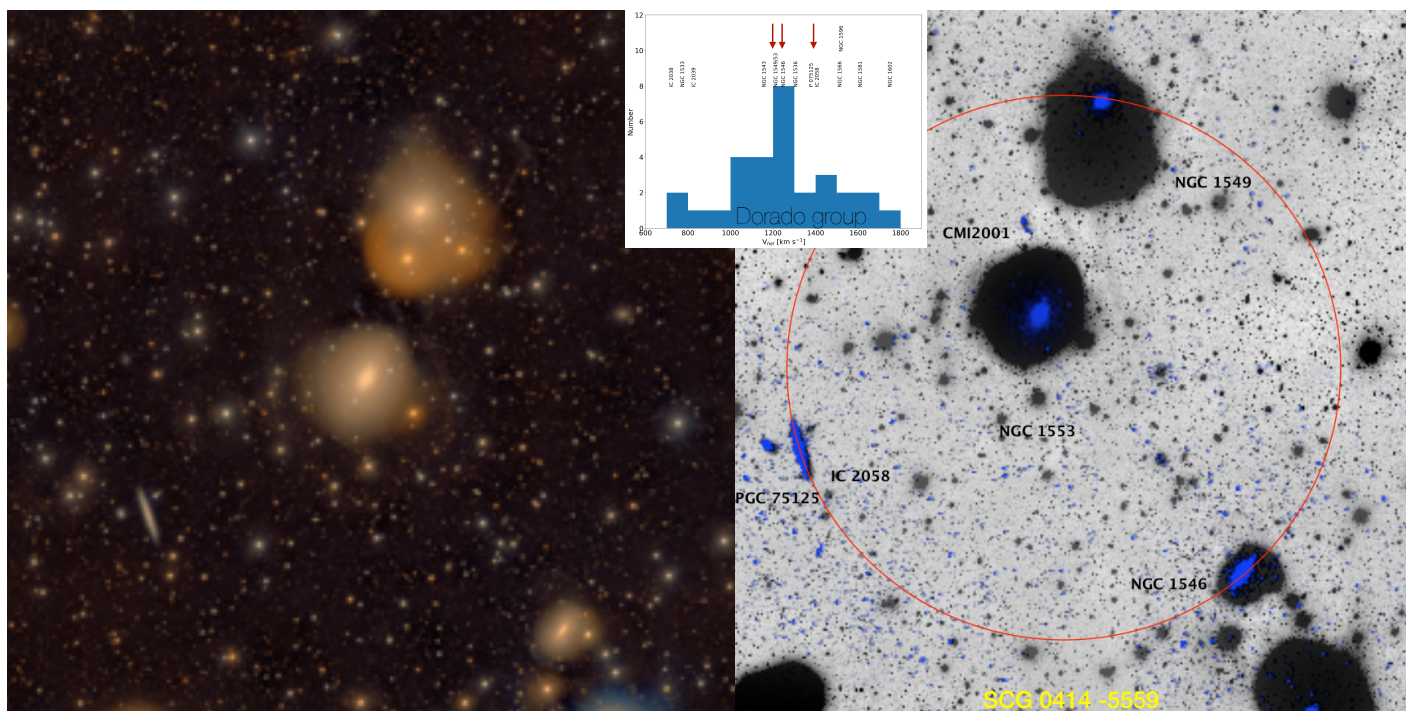


Fig. 12. The compact group SCG 0414 -5559. The left panel shows the colour composite VST image of the Dorado group centre (North is on the top and East to the left). The field of view is 51:77 \times 47:52. The SCG is at the centre of the Dorado members velocity distribution in the Kourkchi & Tully (2017) group definition (central panel). The colour RGB image is created adopting the Lupton et al. (2004) scheme, using the r -band image as R channel input, the g -band as B channel input, and the average image between r and g bands as G channel input. Notice faint shell/ripples structures in NGC 1549 and NGC 1553 (see Malin & Carter 1983) and in the south-east side of NGC 1546. In the right panel an unsharp mask of the SCG is shown. In red is drawn the circle that encloses the compact group, SCG 0414-5559, identified by Iovino (2002, see her Figure 3 and Table 1). In addition to galaxies forming the compact group we labelled PGC 75125, a physical companion of IC 2058 (see e.g. Elagali et al. 2019) and CMI2001, not present in Iovino (2002). Our B, C, D, E UVIT fields are superposed to the unsharp masking of the g -band VST image in order to show extension and distribution of the FUV emission within the compact group members.

any, in LTGs (see e.g. Schweizer & Seitzer 1992). The presence of shells/ripples plus H II regions in the central spiral like structure of NGC 1546 (Ram2020) make this galaxy a borderline object between ETGs and LTGs. The morphological type ($T=-0.4$) and the classification by Comerón et al. (2014) is appropriated.

The radial extension on the VST image of NGC 1546, NGC 1549, NGC 1553 is larger than FUV.CaF2 emission radius by 2.3, 3.2 and 3.4 times in g and by 2.1, 3.5 and 3.5 in r band (Table 4). At odds, the FUV.CaF2 emission of IC 2058 has a radius of 3/2 comparable to the galaxy g band extension (1.1

times) but larger than r band extension which is 0.7 times the FUV ones.

At the light of the VST image, the structure shown by PGC 75125, the physical companion of IC 2058, in FUV.CaF2 (Figure 9) reveals to be either a warped disk or a bar-like structure which is embedded in a spheroidal halo. The optical radii reported in Table (Table 4) are 0:62 and 0.57 in g and r bands, respectively, and 0:42 in FUV.CaF2 at $\mu_{FUV,CaF2} = 29$ mag arcsec $^{-2}$, i.e. the extension in optical PGC 75125 is 1.5 times

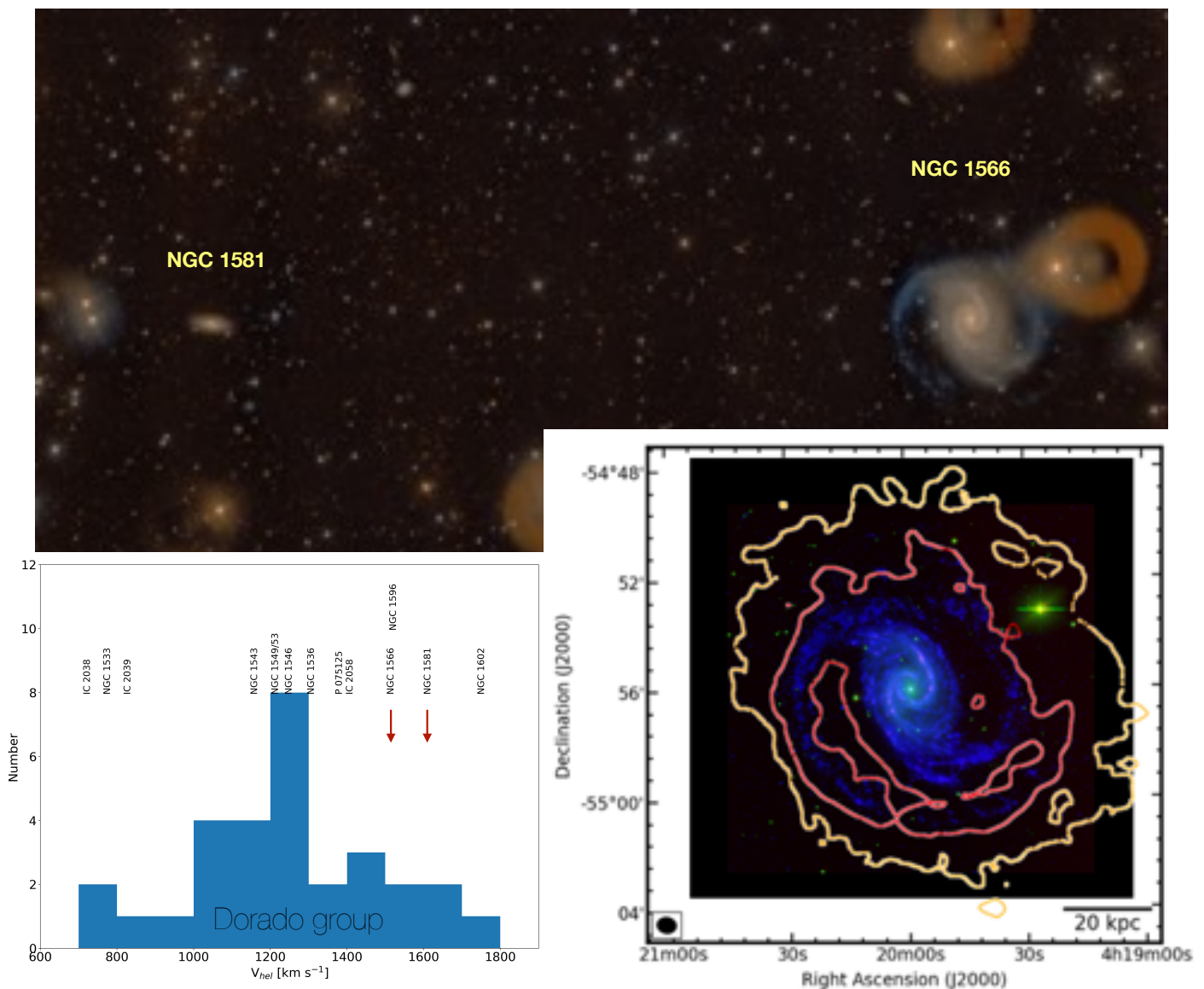


Fig. 13. NGC 1566 and NGC 1581. In the top panel is shown the VST image colour composite image (RGB as in Figure 12) of NGC 1566 and NGC 1581 members (North is on the top and East to the left, FoV=60'80×31'37). Their projected separation is 40.84', while they are separated by 96 km s^{-1} , as shown in the bottom left panel. The bottom right panel shows that the FUV emission of NGC 1566 (13'×13' see Figure 10) extends up to the outer column density of H I at $3.7 \times 10^{20} \text{ cm}^{-2}$ (red) and, especially in the North region, almost to $0.6 \times 10^{20} \text{ cm}^{-2}$ (orange) reported by Elagali et al. (2019).

larger than in FUV.CaF2. We conclude that the compact group members do not show signature of XUV features.

6.0.2. NGC 1566 and NGC 1581

The top panel of Figure 13 shows the VST colour composite image of NGC 1566 and NGC 1581. The projected separation between these galaxies, 210 kpc, is quite large although the recession velocity separation, $\Delta V_{hel} = 96$, is km s^{-1} (bottom left panel of Figure 13) compatible with galaxies being associated.

The UVIT field F includes NGC 1566. NGC 1581 was not observed neither by GALEX nor by UVIT. The grand design spiral NGC 1566 dominates the FUV emission of the Dorado group (Table 3, see also Figure 2). It extends up to $1.65 \times R_{26.5}$ and $0.83 \times R_{29g}$ and is similar to R_{28r} (Table 4). The bottom right

panel of Figure 13 shows that the FUV.CaF2 emission extends almost up to the H I column density of $3.7 \times 10^{20} \text{ cm}^{-2}$, marked by the red contours.

6.0.3. NGC 1596 and NGC 1602

The radial velocities of NGC 1596 and NGC 1602 differ by 230 km s^{-1} as shown by the red arrows in the bottom right panel of Figure 14. The left panel of this Figure shows a colour-composite image of the pair. NGC 1602 is enclosed in a halo stretched towards the NGC 1596 halo.

UVIT FUV.CaF2 observations (Figure 11) show that the two galaxies are sharply separated and without any outer halo. However, the extra-planar features shown by adaptive smoothing applied to the FUV.CaF2 image (bottom right panel of Figure 11) may trace the H I connection (Chung et al. 2006) between the two galaxies shown in the top left panel of Figure 14 in which

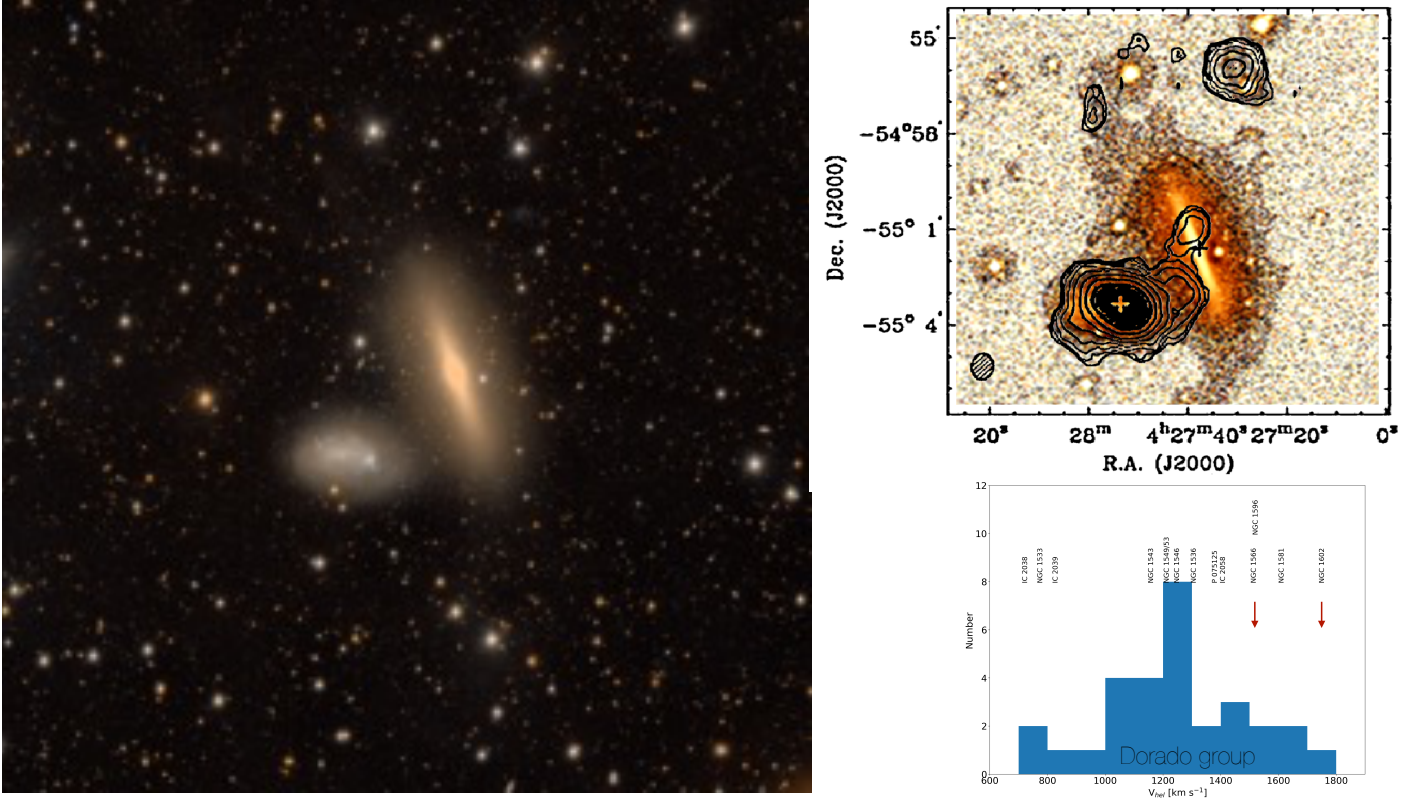


Fig. 14. The physical pair NGC 1596/NGC 1602. In the redshift space these galaxies are separated by 230 km s^{-1} , as shown by the bottom right panel. The VST colour composite image (RGB as in Figure 12) of the pair (left panel, North on is the top and East to the left, FoV= $17'34 \times 17'$) shows that NGC 1602 outskirts appear distorted and, in projection, roughly in contact with NGC 1596, as well as H I contour levels (4, 6, 9, 13.5, 20.3, 30.5, 45.7, 68.6, 102.8 and $154.2 \times 10^{19} \text{ cm}^{-2}$) by Chung et al. (2006) shown in the top right panel. These contours are superposed to our VST unsharp masked image in the top right panel. Crosses indicate the optical centres of the two galaxies, and the synthesized beams ($49.9 \times 37.6 \text{ arcsec}^2$) are also shown at the bottom left of this panel. Similar results for H I are in Figure 14 of Elagali et al. (2019).

Table 4. Radial extension of targets in FUV, CaF2, I, g and r bands

Galaxy	FUV, CaF2 R_{30} [arcmin]	CGS $R_{26.5}$ [arcmin]	VST R_{29g} [arcmin]	VST R_{28r} [arcmin]
IC 2038	1.5^1	...	1.1^{3*}	1.0^{3*}
IC 2039	0.3^1	...	1.0^{3*}	0.6^{3*}
NGC 1533	1.5^1	1.63	5.2^3	4.3^3
NGC 1546	1.7	2.81	4.0^4	3.5^4
NGC 1549	2.0	2.65	6.5^4	7.1^4
NGC 1553	2.0	7.23	6.7^4	6.2^4
IC 2058	3.2	...	3.4^4	2.3^4
PGC 75125	0.4^2	...	0.6^4	0.6^4
NGC 1566	6.7	4.06	8.0^4	6.5^4
NGC 1596	1.3	3.02	6.0^4	5.5^4
NGC 1602	0.8	...	3.6^4	3.6^4

Notes. Col. 1 gives the galaxy identification; Col. 2 reports the semi-major axis R_{30} i.e. the extension of the galaxy at $\mu_{FUV, CaF2} = 30 \text{ mag arcsec}^{-2}$ measured along the FUV, CaF2 luminosity profile. Correspondingly col. 3 provides $R_{26.5}$, the radius at $26.5 \text{ mag arcsec}^{-2}$, derived from I-band by CGS (Ho et al. 2011); Col.s 4 and 5 give R_{29g} and R_{28r} , the semi-major axis the galaxy luminosity profile at 29 and 28 mag arcsec^{-2} in the g and r bands, respectively. Notes:¹ data are from Ram2021; ² the radius for PGC 75125 refers to $\mu_{FUV, CaF2} = 29 \text{ mag arcsec}^{-2}$; ³ data are from Cattapan et al. (2019); ⁴ data are from Ragusa et al. (2022 in preparation). * The radii for IC 2038 and IC 2039 in columns 5 and 6 refer to $\mu_g = 25 \text{ mag arcsec}^{-2}$ and $\mu_r = 24 \text{ mag arcsec}^{-2}$, respectively.

the neutral gas contour are overlaid. The on-going interaction between these two Dorado members distorts their halos as evidenced by the unsharp masking of the VST image.

The radius is about $1'3$ at $\mu_{FUV, CaF2} = 30 \text{ mag arcsec}^{-2}$ for NGC 1596. The optical emission from VST of NGC 1596 is $5'5$ at $\mu_g = 29 \text{ mag arcsec}^{-2}$ and $6'$ at $\mu_r = 28 \text{ mag arcsec}^{-2}$ indicat-

ing that the optical emission is 4.6 and 4.23 times larger than the FUV, CaF2 emission. NGC 1602 at $\mu_{FUV, CaF2} = 30 \text{ mag arcsec}^{-2}$ the radius of $0'8$, i.e 4.5 times smaller than both the R_{29g} and R_{28r} radii from VST frames (see Table 4). None of these galaxies host a XUV disk.

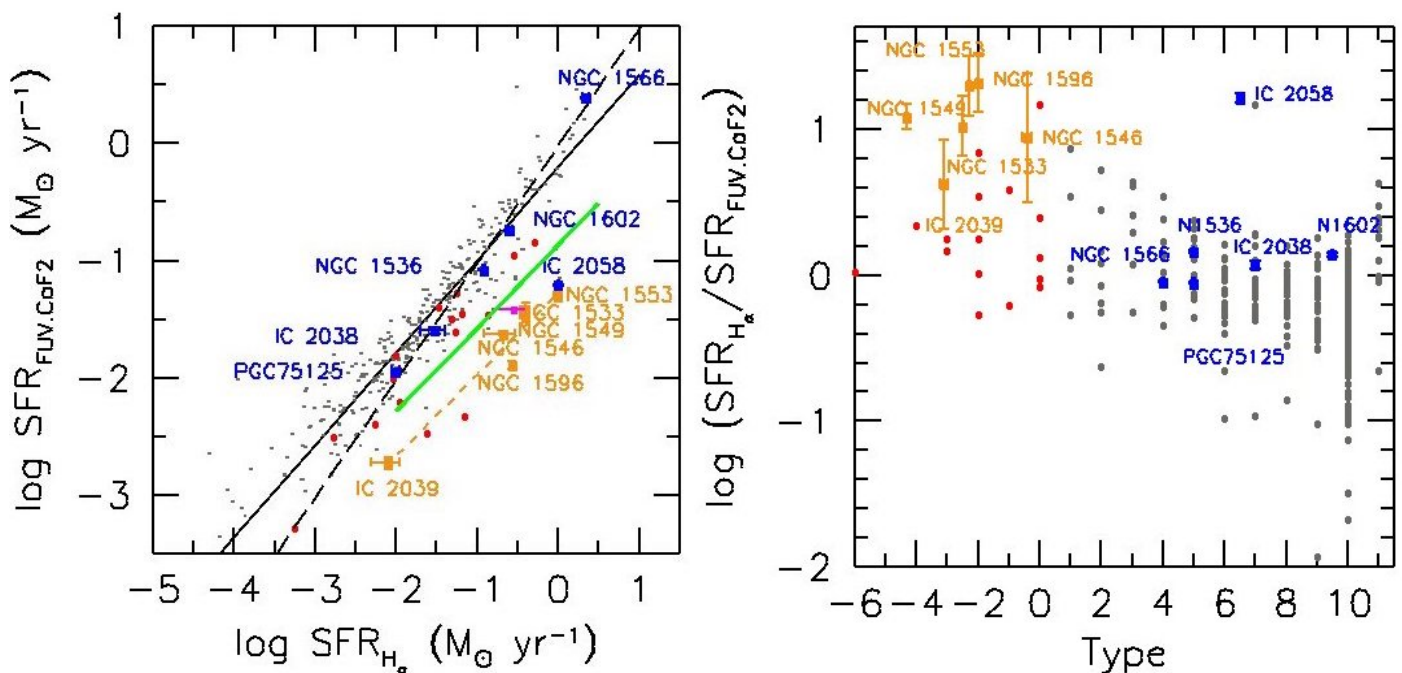


Fig. 15. (Left panel): Comparison between SFR derived from $\text{H}\alpha$ and FUV.CaF2 luminosities. The Dorado sample is plotted with orange (ETG) and blue (LTG) squares. For comparison, we plot Lee et al. (2009, their Table 2) sample with red (ETG) and gray (LTG) dots. The magenta dot shows NGC1533 as derived using SFR from $\text{H}\alpha$ by Kaisina et al. (2012) and from FUV.CaF2 measured in this work. All measures account for Galactic extinction, but internal dust attenuation has not been modelled and accounted for. The black solid and dashed lines show the Lee et al. (2009) relation and the one-to-one correspondence, respectively. The solid green and orange-dashed lines are the regression fit of the entire Dorado sample (equation 3) and of the ETGs members (equation 2), respectively. (Right panel): Ratio of SFR from $\text{H}\alpha$ and FUV.CaF2 versus galaxy morphological type.

We may summarize, the discussion about FUV.CaF2 extension with respect to optical and H I observations as follows:

- The radius of the FUV.CaF2 emission in Dorado ETGs is several times smaller than the optical one as measured either by VST or CGS. This is also the case of NGC 1533 (Ram2021).
- Since the central FUV.CaF2 emission is always consistent with a disk structure, the dissipative processes triggered the recent SF and exhausted the H I in NGC 1549 and NGC 1553 not revealed by the Elagali et al. (2019, see their Figure 14) mosaic of the Dorado group.
- In the periphery of SGC 0414-5559, i.e NGC 1546 and in the pair IC 2058/PGC 75125, the FUV.CaF2 emission is coupled with H I emission (Kilborn et al. 2005; Elagali et al. 2019) and on-going SF (see also Rampazzo et al. 2021).
- In LTGs the FUV.CaF2 and optical VST radii are comparable like IC 2058, NGC 1536 and NGC 1566. Larger FUV.CaF2 extension, XUV disks, are detected in IC 2038 (Ram2021). In NGC 1566 the H I gas emission extends well beyond the the FUV.CaF2 radius measured in the present study (Table 4). The fact that in NGC 1566 both optical and the FUV.CaF2 are of similar size may indicate that the SF drops well before the H I extension.
- The distortion revealed by VST images in the outskirts of NGC 1602 superposes to the H I pipeline emission that connects it to NGC 1596 (Bureau & Chung 2006; Chung et al. 2006) and may feed its recent SF detected by UVIT.

7. SFR from FUV.CaF2 flux versus $\text{H}\alpha$ flux

In this section we compare the SFR of Dorado members as derived from $\text{H}\alpha$ (Ram2020) with that obtained from the

FUV.CaF2 luminosities (Section 4.2). In the comparison we include also members of the NGC 1533 Dorado substructure previously analyzed by Ram2021, thus covering most of the backbone of the Dorado group. We also compare the SFRs of Dorado members with that of galaxies in the Local Volume (LV) (Lee et al. 2009; Karachentsev & Kaisina 2013)

Regarding the comparison between the SFR obtained from different indicators, we recall some critical points discussed by Bianchi (2011). First of all, UV probes ages up to hundreds of Myr, while $\text{H}\alpha$ traces ionizing photon by O and early B stars, i.e. significantly younger ages (Section 4.2 and references therein). Therefore, the Kennicutt et al. (2009) relations are a good approximations for constant average SFR ($t > 10$ Gyr). Second, UV fluxes are affected by reddening more severely than optical fluxes, and, furthermore, dust properties and extinction vary with the local stellar environment. Accurate modeling of galaxy properties from UV data must also account for internal extinction, in particular for LTGs (Bianchi et al. 2017, Table 1).

In Figure 15 (left panel) we compare the SFR obtained from $\text{H}\alpha$ (Ram2020) and FUV.CaF2 fluxes (Table 3). Both fluxes are corrected for the foreground extinction as described in Section 4.2. No correction for internal extinction has been applied. Figure 15 shows that all Dorado LTGs ($T > 0$, blue squares) are essentially distributed along the 1:1 line (black-dashed line in the left panel), except for the edge-on IC 2058, where neglecting internal extinction correction can significantly alter the result.

For the Dorado ETGs ($-5 \leq T \leq 0$ orange squares), instead, $\text{SFR}_{\text{FUV.CaF2}}$ is at least 1 dex lower than $\text{SFR}_{\text{H}\alpha}$. Such marked difference is also seen in the right panel of Figure 15 where the ratio $[\text{SFR}_{\text{H}\alpha} / \text{SFR}_{\text{FUV.CaF2}}]$ is plotted as a function of the morphological type.

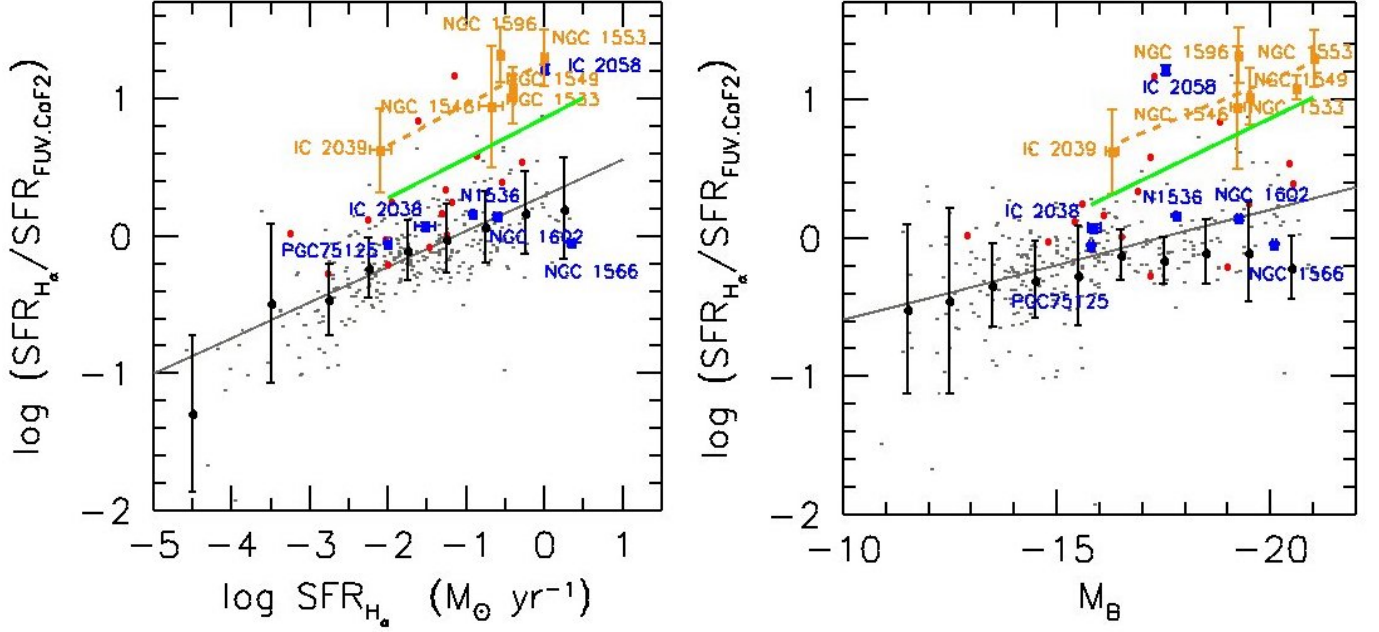


Fig. 16. Ratio between the SFR from $H\alpha$ and FUV.CaF2 luminosities in logarithmic scale versus the SFR from $H\alpha$ (left panel) and the absolute B-band magnitude (right panel). Symbols used are the same as in Figure 15. Black dots are average values of the sample of Lee et al. (2009, their Table 2). Solid grey lines are the linear least squares fits by Lee et al. (2009). The solid green and orange dashed lines are the regression fit of the entire Dorado sample (equation 4 in left panel and equation 6 in the right panel) and for the ETGs (equation 5 in left panel and equation 7 in the right panel), respectively.

Given that the Dorado’s ETGs define a well separated locus from the LTGs, and a clear trend (roughly parallel to that of the LTGs, but more than 1dex offset), we fit the relation between their SFR values and find:

$$\log(SFR_{FUV,CaF2}) = 0.70 \times \log(SFR_{H\alpha}) - 1.26 \quad (2)$$

with a correlation index= 0.97. The regression fit is shown as a dashed orange line in Figure 15.

For comparison, we also plot in Figure 15 the sample of about 300 local volume (<11 Mpc) galaxies by Lee et al. (2009), who used GALEX UV data and ground-based $H\alpha$ measurements to derive SFR; these authors account for the foreground but not for internal extinction, as for our data-set. Their sample included LTGs (the majority, gray dots in our figure) and a few ETGs (red dots). Lee et al. (2009) derived a relation from their whole sample, which we report the left panel of in Figure 15 as a solid black line. A few facts appear evident from Figure 15. Lee et al. (2009) relation is driven by their LTGs (more numerous in their sample), and it does not strongly differ from the distribution of the Dorado’s LTGs; these seem more closely aligned along the 1:1 line (again excluding the edge-on case, that would require a large extinction correction); we do not derive a formal regression fit for the Dorado LTGs due to the scarcity of the sample. The ETGs in Lee et al. (2009) sample (red dots in Figure 15) span a broad locus, from their relation derived for the whole sample all the way to the locus of the Dorado ETGs. Karachentsev & Kaisina (2013) had also studied the SFR of the LV galaxies using $H\alpha$ and FUV measures, and noted that ETGs show a large dispersion in SFR.

The $SFR_{FUV,CaF2}$ versus $SFR_{H\alpha}$ trend for the entire Dorado sample, shown in Figure 15 by a green continuous line, is represented by the relation:

$$\log(SFR_{FUV,CaF2}) = 0.77 \times \log(SFR_{H\alpha}) - 0.43 \quad (3)$$

with correlation index= 0.84. The comparison of this relation with the general relation by Lee et al. (2009) and with the relation for Dorado’s ETGs simply reflects the differing composition of the samples, i.e. the relative content of ‘classical’ LTGs vs ETGs. The relations are approximately parallel, as expected because they trace a gradient of SFR intensity across the sample.

This is further evidenced in Figure 16 where the trend of the $\log(SFR_{H\alpha}/SFR_{FUV})$ ratio is shown as a function of the $\log(SFR_{H\alpha})$ (left panel) and the absolute B-band magnitude, M_B (right panel) in Table 1. We fit our values obtaining relations, for the entire Dorado sample (equation 4, 6) and for ETGs (equation 5, 7). The relations plotted in the left panel of Figure 16 are:

$$\log(SFR_{FUV,CaF2}/SFR_{H\alpha}) = 0.24 \times \log(SFR_{H\alpha}) + 0.46 \quad (4)$$

$$\log(SFR_{FUV,CaF2}/SFR_{H\alpha}) = 0.30 \times \log(SFR_{H\alpha}) + 1.26 \quad (5)$$

while in the right panel are:

$$\log(SFR_{FUV,CaF2}/SFR_{H\alpha}) = -0.15 \times M_B - 2.11 \quad (6)$$

$$\log(SFR_{FUV,CaF2}/SFR_{H\alpha}) = -0.13 \times M_B - 1.40 \quad (7)$$

If we exclude IC 2058, Dorado LTGs roughly align along the $SFR_{H\alpha}$ vs. $SFR_{FUV,CaF2}$ one-to-one correspondence line as shown in Figure 15. We conclude that the relation between the two SFR indicators for LTGs (especially at $\log(SFR) \gtrsim -2.5$) is essentially consistent across different LV environments, while ETGs can depart by over one order of magnitude.

We believe it is unlikely that internal extinction in LTGs could account for the large discrepancy between SFR_{FUV} vs $SFR_{H\alpha}$. Mazzei et al. (2014a,b) have performed full modeling with smoothed particle hydrodynamic simulations with chemometric implementation (SPH-CPI) of two galaxies, one in our sample (NGC 1533) and one with similar characteristics (NGC1543, Marino et al. (see 2011a), Ram2020). The simulations included self-gravity of gas, stars and dark matter, radiative cooling, hydro-dynamical pressure, shock heating, viscosity, star formation and feedback from evolved stars and type II supernovae and chemical enrichment, and matched all the observed properties of the galaxies. Their results showed that internal reddening could account for a factor of 2 correction to the SFR, at most.

We argue that the LTGs versus ETGs behaviour shown by Figure 15 and 16 is not surprising, given the different modality of SF which is residual in ETGs at odds with LTGs. SF episodes in ETGs cannot support a constant SF for 10^8 yr or longer (1 Gyr), as required for SFR_{UV} Kennicutt (1998) calibration. Moreover, as Kennicutt & Evans (2012, and references therein) reported, the systematic dependence of the $H\alpha/UV$ ratio in Figure 15 and 16 may be produced by temporal variations in SFRs. Such variations of SFR are typical of ETGs as shown by SPH-CPI simulations (see Mazzei et al. 2019, and references therein). Since the global Dorado $H\alpha$ vs FUV SFR relation is driven by the ETGs, i.e. by the Dorado evolutionary status, we argue that FUV vs. $H\alpha$ SFR relation may be caused by the mix of different galaxy types.

8. Summary and conclusions

We observed with the far-ultraviolet channel (FUV.CaF2) (1300-1800 Å) of ASTROSAT-UVIT 7 fields mapping Dorado, a nearby and still clumpy group, extending for about 10 square degrees in the Southern Hemisphere. We present the study of its core region, identified by the compact group SCG 0414-5559 (Iovino 2002), the NGC 1566/NGC 1581 and the NGC 1596/NGC 1602 substructures, these latter observed for the first time in FUV. We included in the analysis also the Dorado South-West NGC 1533 substructure previously investigated with UVIT and the same filter in Ram2021.

All galaxies observed are detected in FUV.CaF2. We revealed an inner ring in NGC 1549, not detected in optical bands, and a ring in NGC 1546 which adds to FUV rings found in NGC1533 and NGC1543 by previous UV studies (see Marino et al. 2011a, and Ram2021). Simulations show these resonance rings originate by mergers, fly-by encounters and, in general, galaxy-galaxy interactions (Mazzei et al. 2014a,b; Eliche-Moral et al. 2018; Mazzei et al. 2018, 2019, 2022). Structural asymmetries in the FUV.CaF2 image of NGC 1566, PGC 75125 and [CMI2001]4136-01 are additional signatures of interactions. In both IC 2058 and NGC 1596 the smoothed FUV.CaF2 emission enhances the presence of extra-planar features not revealed in $H\alpha$ (Ram2020).

We analyzed the galaxy morphology, the surface brightness profiles and obtained integrated magnitudes. We fit the surface brightness profiles adopting a single Sérsic law. Excluding NGC 1602, strongly irregular in the FUV.CaF2 band, the range of the Sérsic index, $0.76 \pm 0.02 \leq n \leq 2.86 \pm 0.28$, indicates the presence of a disk in all the galaxies (see Rampazzo et al. 2017), and suggests that dissipation mechanisms have operated in shaping the FUV.CaF2 structure, even in the gas poor ETGs like NGC 1553 and NGC 1549.

We used deep, g and r wide field VST images to investigate the presence of XUV disk by comparison with the FUV.CaF2 extension. We found that in ETGs the FUV.CaF2 emission is several times less extended than the optical one. At odds, LTGs have similar FUV.CaF2 and optical dimensions. IC 2038 is consistent with having a XUV disk (Ram2021).

The residual SF in ETGs of Dorado is proven by their FUV emission, shaped in a disk, and detection of $H\text{II}$ regions in a significant fraction of them (Ram2020). The SFR estimates from $H\alpha$ and UV give consistent results for LTGs. The only exception is IC 2058 which is seen edge-on. At odds, the SFR estimate from $H\alpha$ of Dorado ETGs is at least 10 times higher than the UV estimate. We derived the relations describing the $SFR_{FUV,CaF2}$ and the $SFR_{H\alpha}$ trends for the entire Dorado backbone (equations 3, 4 and 6) and for ETGs members separately (equations 2, 5 and 7).

ETGs in Dorado are numerous and drive the SFR relations we derived. We suggest that Dorado $SFR_{H\alpha}$ versus $SFR_{FUV,CaF2}$ relation marks the group evolutionary status. On the other hand, SF episodes in ETGs cannot support a underlying, constant SFR as required by general calibrations (Kennicutt 1998), as shown by SPH-CPI simulations (Mazzei et al. 2022, and reference therein).

Our analysis in the short wavelength range (FUV.CaF2) of Dorado galaxy members confirms the active evolutionary status of this group indicated by optical (Malin & Carter 1983), radio (Kilborn et al. 2005; Elagali et al. 2019), and $H\alpha$ observations (Ram2020).

Acknowledgements. The UVIT project is collaboration between the following institutes from India: Indian Institute of Astrophysics (IIA), Bengaluru, Inter University Centre for Astronomy and Astrophysics (IUCAA), Pune, and National Centre for Radioastrophysics (NCRA) (TIFR), Pune, and the Canadian Space Agency (CSA). The detector systems are provided by the Canadian Space Agency. The mirrors are provided by LEOS, ISRO, Bengaluru and the filter-wheels drives are provided by IISU, ISRO, Trivandrum. Many departments from ISAC, ISRO, Bengaluru have provided direct support in design and implementation of the various sub-systems. Data from Extragalactic Database (NED) and NASA's Astrophysics Data System (ADS) are also used in this paper. We acknowledge the usage of the HyperLeda database (<http://leda.univ-lyon1.fr>).

References

- Abadi, M. G., Moore, B., & Bower, R. G. 1999, MNRAS, 308, 947
 Bai, Y., Zou, H., Liu, J., & Wang, S. 2015, The Astrophysical Journal Supplement Series, 220, 6
 Bender, R., Doebereiner, S., & Moellenhoff, C. 1988, A&AS, 74, 385
 Bianchi, L. 2011, Ap&SS, 335, 51
 Bianchi, L., Shiao, B., & Thilker, D. 2017, ApJS, 230, 24
 Bigiel, F., Leroy, A., Seibert, M., et al. 2010, ApJ, 720, L31
 Boselli, A. & Gavazzi, G. 2014, Astronomy and Astrophysics Review, 22, 74
 Bressan, A., Panuzzo, P., Buson, L., et al. 2006, ApJ, 639, L55
 Bureau, M. & Chung, A. 2006, MNRAS, 366, 182
 Buta, R. J., Sheth, K., Athanassoula, E., et al. 2015, ApJS, 217, 32
 Capaccioli, M., Spavone, M., Grado, A., et al. 2015, A&A, 581, A10
 Cattapan, A., Spavone, M., Iodice, E., et al. 2019, ApJ, 874, 130
 Chung, A., Koribalski, B., Bureau, M., & van Gorkom, J. H. 2006, MNRAS, 370, 1565
 Comerón, S., Salo, H., Laurikainen, E., et al. 2014, A&A, 562, A121
 Davis, M. & Geller, M. J. 1976, ApJ, 208, 13
 de Vaucouleurs, A., Corwin, H. G., Buta, R. J., et al. 1992, The Observatory, 112, 127
 de Vaucouleurs, G. 1953, AJ, 58, 30
 Diaferio, A., Geller, M. J., & Ramella, M. 1994, AJ, 107, 868
 Díaz-Giménez, E., Zandivarez, A., & Mamon, G. A. 2021, MNRAS, 503, 394
 Dressler, A. 1980, ApJ, 236, 351
 Ebeling, H., White, D. A., & Rangarajan, F. V. N. 2006, MNRAS, 368, 65
 Elagali, A., Staveley-Smith, L., Rhee, J., et al. 2019, MNRAS, 487, 2797
 Eliche-Moral, M. C., Rodríguez-Pérez, C., Borlaff, A., Querejeta, M., & Tapia, T. 2018, A&A, 617, A113

- Firth, P., Evstigneeva, E. A., Jones, J. B., et al. 2006, *MNRAS*, 372, 1856
- Freeman, K. C. 1970, *ApJ*, 160, 811
- Gavazzi, G., Consolandi, G., Pedraglio, S., et al. 2018, *A&A*, 611, A28
- George, K., Poggianti, B. M., Gullieuszik, M., et al. 2018, *MNRAS*, 479, 4126
- Gil de Paz, A., Boissier, S., Madore, B. F., et al. 2007, *ApJS*, 173, 185
- Gil de Paz, A., Thilker, D. A., Bianchi, L., et al. 2008, in *Astronomical Society of the Pacific Conference Series*, Vol. 396, *Formation and Evolution of Galaxy Disks*, ed. J. G. Funes & E. M. Corsini, 197
- Gunn, J. E. & Gott, J. Richard, I. 1972, *ApJ*, 176, 1
- Hester, J. A., Seibert, M., Neill, J. D., et al. 2010, *ApJ*, 716, L14
- Ho, L. C., Li, Z.-Y., Barth, A. J., Seigar, M. S., & Peng, C. Y. 2011, *The Astrophysical Journal Supplement Series*, 197, 21
- Hota, A., Devaraj, A., Pradhan, A. C., et al. 2021, *Journal of Astrophysics and Astronomy*, 42, 86
- Iovino, A. 2002, *AJ*, 124, 2471
- James, P. A., Shane, N. S., Beckman, J. E., et al. 2004, *A&A*, 414, 23
- Jedrzejewski, R. I. 1987, *MNRAS*, 226, 747
- Jeong, H., Yi, S. K., Bureau, M., et al. 2009, *MNRAS*, 398, 2028
- Kaisina, E. I., Makarov, D. I., Karachentsev, I. D., & Kaisin, S. S. 2012, *Astrophysical Bulletin*, 67, 115
- Kantharia, N. G., Ananthakrishnan, S., Nityananda, R., & Hota, A. 2005, *A&A*, 435, 483
- Karachentsev, I. D. & Kaisina, E. I. 2013, *AJ*, 146, 46
- Kendall, S., Clarke, C., & Kennicutt, R. C. 2015, *MNRAS*, 446, 4155
- Kennicutt, Robert C., J. 1998, *ARA&A*, 36, 189
- Kennicutt, Robert C., J., Hao, C.-N., Calzetti, D., et al. 2009, *ApJ*, 703, 1672
- Kennicutt, R. C. & Evans, N. J. 2012, *ARA&A*, 50, 531
- Kilborn, V. A., Forbes, D. A., Barnes, D. G., et al. 2009, *MNRAS*, 400, 1962
- Kilborn, V. A., Koribalski, B. S., Forbes, D. A., Barnes, D. G., & Musgrave, R. C. 2005, *MNRAS*, 356, 77
- Kourkchi, E. & Tully, R. B. 2017, *ApJ*, 843, 16
- Kumar, A., Ghosh, S. K., Kamath, P. U., et al. 2012, in *Society of Photo-Optical Instrumentation Engineers (SPIE) Conference Series*, Vol. 8443, *Space Telescopes and Instrumentation 2012: Ultraviolet to Gamma Ray*, 84434R
- Lee, J. C., Gil de Paz, A., Tremonti, C., et al. 2009, *ApJ*, 706, 599
- Lupton, R., Blanton, M. R., Fekete, G., et al. 2004, *PASP*, 116, 133
- Malin, D. F. & Carter, D. 1983, *ApJ*, 274, 534
- Mamon, G. A. 1992, *ApJ*, 401, L3
- Marino, A., Bianchi, L., Mazzei, P., Rampazzo, R., & Galletta, G. 2014, *Advances in Space Research*, 53, 920
- Marino, A., Bianchi, L., Rampazzo, R., Buson, L. M., & Bettoni, D. 2010, *A&A*, 511, A29
- Marino, A., Bianchi, L., Rampazzo, R., et al. 2011a, *Ap&SS*, 335, 243
- Marino, A., Mazzei, P., Rampazzo, R., & Bianchi, L. 2016, *MNRAS*, 459, 2212
- Marino, A., Plana, H., Rampazzo, R., et al. 2013, *MNRAS*, 428, 476
- Marino, A., Rampazzo, R., Bianchi, L., et al. 2011b, *MNRAS*, 411, 311
- Martin, D. C., Fanson, J., Schiminovich, D., et al. 2005, *ApJ*, 619, L1
- Mazzei, P., Marino, A., & Rampazzo, R. 2014b, *ApJ*, 782, 53
- Mazzei, P., Marino, A., Rampazzo, R., Galletta, G., & Bettoni, D. 2014a, *Advances in Space Research*, 53, 950
- Mazzei, P., Marino, A., Rampazzo, R., et al. 2018, *A&A*, 610, A8
- Mazzei, P., Rampazzo, R., Marino, A., et al. 2019, *ApJ*, 885, 165
- Mazzei, P., Rampazzo, R., Marino, A., et al. 2022, *ApJ*, 927, 124
- Meert, A., Vikram, V., & Bernardi, M. 2015, *MNRAS*, 446, 3943
- Morrissey, P., Conrow, T., Barlow, T. A., et al. 2007, *ApJS*, 173, 682
- Oh, S. H., Kim, W.-T., & Lee, H. M. 2015, *ApJ*, 807, 73
- Poggianti, B. M., von der Linden, A., De Lucia, G., et al. 2006, *ApJ*, 642, 188
- Postma, J., Hutchings, J. B., & Leahy, D. 2011, *PASP*, 123, 833
- Postma, J. E. & Leahy, D. 2017, *PASP*, 129, 115002
- Postma, J. E. & Leahy, D. 2020, *PASP*, 132, 054503
- Rampazzo, R., Ciroi, S., Mazzei, P., et al. 2020, *A&A*, 643, A176
- Rampazzo, R., Marino, A., Tantalò, R., et al. 2007, *MNRAS*, 381, 245
- Rampazzo, R., Mazzei, P., Marino, A., et al. 2021, *Journal of Astrophysics and Astronomy*, 42, 31
- Rampazzo, R., Mazzei, P., Marino, A., et al. 2018, *Ap&SS*, 363, 80
- Rampazzo, R., Mazzei, P., Marino, A., et al. 2017, *A&A*, 602, A97
- Rampazzo, R., Panuzzo, P., Vega, O., et al. 2013, *MNRAS*, 432, 374
- Ribeiro, A. L. B., de Carvalho, R. R., Capelato, H. V., & Zepf, S. E. 1998, *ApJ*, 497, 72
- Roberts, I. D., van Weeren, R. J., McGee, S. L., et al. 2021, *A&A*, 652, A153
- Rossa, J. & Dettmar, R. J. 2003, *A&A*, 406, 493
- Ryan-Weber, E. V., Meurer, G. R., Freeman, K. C., et al. 2004, *AJ*, 127, 1431
- Ryan-Weber, E. V., Webster, R. L., & Staveley-Smith, L. 2003, *MNRAS*, 343, 1195
- Schipani, P., Noethe, L., Arcidiacono, C., et al. 2012, *Journal of the Optical Society of America A*, 29, 1359
- Schweizer, F. & Seitzer, P. 1992, *AJ*, 104, 1039
- Smith, R. J., Lucey, J. R., Hammer, D., et al. 2010, *MNRAS*, 408, 1417
- Spavone, M., Capaccioli, M., Napolitano, N. R., et al. 2017, *A&A*, 603, A38
- Tandon, S. N., Subramaniam, A., Girish, V., et al. 2017, *AJ*, 154, 128
- Thilker, D. A., Bianchi, L., Meurer, G., et al. 2007, *ApJS*, 173, 538
- Thilker, D. A., Bianchi, L., Schiminovich, D., et al. 2010, *ApJ*, 714, L171
- Vulcani, B., Poggianti, B. M., Moretti, A., et al. 2021, *ApJ*, 914, 27
- Werk, J. K., Putman, M. E., Meurer, G. R., et al. 2010, *AJ*, 139, 279